Validation of MODIS Evapotranspiration product (MOD16) for an agricultural region in Austria

---

Institute of Surveying, Remote Sensing and Land Information
University of Natural Resources and Life Sciences, Vienna

Master's Thesis

Requirements for the academic degree of

Dipl.-Ing.

for the Master Programme
Water Management and Environmental Engineering

by

Anastasios-Petros Kazamias

March, 2016

1st Supervisor: Univ.Prof. Dr.rer.nat. Clement Atzberger
2nd Supervisor: Dr. Francesco Vuolo

Page intentionally left blank

Declaration

I hereby declare and confirm that this Master's thesis is entirely the result of my own original work and I have documented all sources and material used. I further declare that this or similar work has not been submitted for credit elsewhere.

Vienna, 26/03/2016

Anastasios-Petros Kazamias

Acknowledgements

This thesis concludes my studies in the Water Management and Environmental Engineering Master Programme at BOKU. Many people have supported me and helped me over the last few years during my studies and I would like to express my gratitude towards them in the next few lines.

Firstly, I would like to thank my two supervisors Univ.Prof. Dr.rer.nat. Clement Atzberger and Dr. Francesco Vuolo. I would especially like to thank Francesco for proposing the topic of this thesis and for always having some time to answer my questions and guide me through the entire thesis-writing process.

Furthermore, I am deeply grateful to my mother for always being there to listen my problems, encourage me and support me during my studies.

Moreover, I would like to thank my girlfriend Marianna and my best friend Fotis that stood next to me during these few years, although they were hundred kilometres far. Their love, unlimited support, continuous encouragement and understanding were key motivations throughout my studies and helped me overcome many difficulties I encountered.

Also, special thanks to all my colleagues and friends in Vienna and Thessaloniki who encouraged me and helped me with different ways during all this time.

Finally, I am grateful to the Greek State Scholarship Foundation (IKY) which awarded me a 2-year full scholarship for my master's studies at the University of Natural Resources and Life Sciences, Vienna.

Abstract

Evapotranspiration (ET) is one of the most important components of the terrestrial ecosystem, linking mass and energy fluxes. Using remotely sensed (RS) data, regional and global scale estimates of ET can be derived and used in numerous applications related to water resources management, crop modelling and climate change studies. One of the readily available operational RS-based ET products is the MODIS global ET (MOD16) at 1 km spatial resolution. This study evaluates the 8-day MOD16 actual ET product over a semi-arid agricultural area located in Lower Austria during the growing season of 2014. The evaluation is performed at a regional scale, against ET maps aggregated at the same spatial and temporal resolution as the MOD16 ET product. These ET maps were generated by an adopted FAO-56 Penman-Monteith approach using high resolution Landsat-8 images and they were validated against Eddy Covariance (EC) measurements, showing a high coefficient of determination (R^2=0.84) and a mean bias error (MBE) of 0.02 mm/hr. The intercomparison between the two ET products showed a low level of agreement for the entire study period with an average R^2 of 0.38 and a systematic underestimation of ET by MOD16 during most of the study period, ranging from 3.09 mm/8day to 7.78 mm/8day. Finally, the MOD16 ET product was evaluated against meteorological data and soil water content measurements to examine the impact of soil water availability on MOD16 ET. The results indicated that the use of MERRA-GMAO relative humidity (RH) does not effectively capture the soil moisture dynamics on ET.

Keywords: Evapotranspiration (ET), Remote sensing, MOD16, Validation, MODIS, Landsat-8

Zusammenfassung

Die Evapotranspiration (ET) ist eine der wichtigsten Komponenten des terrestrischen Ökosystems, die Massenströme und Energieflüsse verknüpft. Durch die Verwendung von Fernerkundungsdaten (RS) können Schätzungen von ET auf regionaler und globaler Ebene angestellt werden, welche in zahlreichen Anwendungsgebieten wie Wasserressourcen-Management, Pflanzenmodellierung und Klimastudien verwendet werden können. Ein leicht verfügbarer betriebliche Fernerkundungsdatensatz ist MODIS global ET (MOD16) mit einer räumlichen Auflösung von 1 km. Diese Studie bewertet das 8-Tage MOD16 tatsächliche ET Produkt über einem landwirtschaftlichen semiariden Gebiet in Niederösterreich während der Vegetationsperiode 2014. Die Evaluierung wird gegen existierende ET-Karten abgeglichen, welche die gleiche räumliche und zeitliche Auflösung haben wie die des MOD16 ET Produkts und auf regionaler Ebene durchgeführt. Diese ET Karten wurden mit einem adaptierten FAO-56 Penman-Monteith-Ansatz unter Verwendung von hochauflösenden Landsat-8-Bilder erzeugt und wurden erst gegen Eddy-Kovarianz (EC) Messungen validiert, mit einem hohen Bestimmtheitsmaß (R^2=0.84) und ein mittlerer Bias Fehler (MBE) von 0.02 mm/hr. Der Vergleich zwischen den beiden ET Produkte zeigte eine geringe übereinstimmung für den gesamten Untersuchungszeitraum mit durchschnittlich R^2 von 0.38 und einer systematischen Unterschätzung der ET durch MOD16 während des größten Teils des Untersuchungszeitraums, die in einem Bereich von 3.09 mm/8Tage bis 7.78 mm/8Tage liegt. Schließlich wurde das MOD16 ET Produkt mit meteorologischen Daten und Wassergehalt-Bodenmessungen kombiniert, um die Auswirkungen von Bodenwasserverfügbarkeit auf MOD16 ET zu untersuchen. Die Ergebnisse zeigten, dass die Verwendung von MERRA-GMAO relative Feuchte (RH) als Substitut der Bodenfeuchte nicht effektiv die Dynamik der Bodenwasserverfügbarkeit auf ET erfassen konnte.

Keywords: Evapotranspiration (ET), Fernerkundung, MOD16, Validierung, MODIS, Landsat-8

Contents

List of Figures

List of Tables

1 Introduction

1.1 Theoretical background

On a global scale, over 60% of land precipitation is water transferred to the atmosphere through evapotranspiration, making it the second largest term in the terrestrial water budget (Dingman, 2001; Glenn et al., 2007). Moreover, the physical process of evapotranspiration is a key element in the soil-plant-atmosphere continuum linking the water balance and the energy balance at the near-surface of the earth through the transport of mass and energy, respectively.

For this reason evapotranspiration can be considered either as a water flux (ET) with mass dimensions, or as an energy flux (LE or λE) with density dimensions. In the second case the water vapour flux is multiplied by the latent heat of vaporization (L or λ).

The process of evapotranspiration (ET) comprises of two sub-processes: evaporation (E) and transpiration (T). Evaporation is the transfer of liquid water into a gaseous state and occurs on the surfaces of open water bodies, vegetation and bare ground. The rate of evaporation is determined by the following four factors: a) the available water for evaporation, b) the available energy at the evaporating surface, c) the operation of diffusion processes in the air above the evaporating surface and d) the surface/vegetation characteristics. Transpiration from a plant involves the withdrawal and transport of water from the soil/aquifer system through plant roots and stem and eventually from the plant leaves into the atmosphere, as part of it's photosynthesis and respiration process. The rate of transpiration depends on the plant physiology, in particular the opening and closing of stomata in the leaves. Because in most of the cases vegetation is present and the two processes operate together, they are generally combined to give the term evapotranspiration (Petropoulos, 2013; Senay et al., 2011).

1.2 ET measurements and modelling

Evapotranspiration can be directly measured by lysimeters, Energy Balance Bowen Ratio stations (EBBR) and Eddy Covariance (EC) flux towers. Also, there are some measurement techniques from which evapotranspiration can be indirectly estimated, such as the pan evaporation technique and the scintillometer. Lysimeter and pan evaporation measurements can only represent a scale of few square meters. The representative spatial scale, or footprint, of EC and EBBR measurements is much larger, ranging from 100 to 200 m. Finally, scintillometers provide measurements over a scale from hundred of meters to kilometres (Wang and Dickinson, 2012).

A quantitative understanding of evapotranspiration is of great importance for water resources allocation and management, climate change studies, irrigation scheduling, crop yield forecasting, weather prediction and drought impact assessment (Dingman, 2001). For all these cases, the amount and rate of ET is required across multiple spatial and temporal scales. Such information are difficult or impractical with direct measurements. The above mentioned techniques can provide accurate ET measurements at a specific location, or "point scale", on the order of few hundred meters, but in most cases the instruments involved are very expensive and scientific personnel is required for their operation, making it difficult to use them routinely. Furthermore, it is difficult to extrapolate these point measurements to a larger scale, such as that of a river basin, region or continent, since ET is highly variable under heterogeneous land surface (McCabe and Wood, 2006). Therefore scientists have developed a number of methods for

estimating ET at various scales ranging from a leaf to a forest stand to a river basin (Senay et al., 2011), using various modelling approaches which are based on the water balance, on the energy balance and empirical methods based on standard meteorological measurements.

The water balance approach involves the application of the water balance equation (Equation 1.1) to the area of interest over a time period Δt and solving the equation for evapotranspiration (ET), if all other terms are known (Dingman, 2001):

$$ET = P + Q_{in} + G_{in} - Q_{out} - G_{out} - \Delta S \tag{1.1}$$

where P is the precipitation, Q_{in} and Q_{out} are the inflows and outflows of surface water, G_{in} and G_{out} are the inflows and outflows of ground water and ΔS is the change in the amount of water in the catchment during Δt. The dimensions of all quantities are of either volume or volume per unit area.

In the energy balance approach the latent heat flux (LE) is determined as the residual of the energy balance equation (Equation 1.2), if all other terms are known. The energy balance equation, without advection, is expressed as:

$$LE = R_n - G - H \tag{1.2}$$

where LE is the latent heat flux (W/m^2), R_n is the net radiation at surface (W/m^2), G is the ground heat flux (W/m^2) and H is the sensible heat flux (W/m^2).

Penman (1948) was the first to describe evaporation from a wet surface combining the energy balance equation with transfer equations for turbulent fluxes. The transfer equations for heat (H) and water vapour (LE) employed in Penman's approach consider the land surface as an electrical analogue, which means that the exchange rate, F, of a quantity (e.g heat, water vapour) between two points A and B is driven by a difference in potential of the quantity, X (e.g. temperature, specific humidity), and controlled by a number of resistances, r, that depend on the local environment and internal properties of the land surface and vegetation (Overgaard et al., 2005; Kalma et al., 2008):

$$F = C\frac{X_B - X_A}{r_{AB}} \tag{1.3}$$

where C is a constant depending on the quantity under consideration.

Furthermore, Penman eliminated the need for surface potentials, which require surface temperature measurements, by assuming that the saturation vapour pressure is a linear function of temperature (Overgaard et al., 2005). Finally, Penman assumed that the only resistance working between the wet surface and the atmosphere was the so-called atmospheric resistance, that depends on wind speed and stability (Moene and van Dam, 2014; Overgaard et al., 2005). Monteith (1965) further developed the Penman method for vegetated surfaces by introducing an additional surface resistance. This resistance depends on the vegetation type, soil moisture conditions and local climate.
The water vapour flux described by the so called Penman-Monteith (PM) method is referred as evapotranspiration (ET), including both transpiration (T) and evaporation (E) from soil and intercepted water. The models based on the Penman-Monteith approach are also called "one-layer" or "big-leaf" models, because they do not distinguish soil evaporation and transpiration, but treat the land surface as one homogeneous surface (Overgaard et al., 2005).

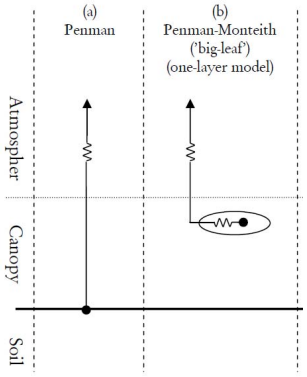

Figure 1.1: Resistance scheme for Penman and Penman-Monteith models (Overgaard et al., 2005).

1.3 Evapotranspiration estimation with remote sensing data

Remotely sensed (RS) data, combined in some form of model or algorithm, can be used to estimate ET at a variety of spatial and temporal scales. Given the fact that measurements of ET are available only over point or field spatial scales, remotely sensed data have been recognized as the only viable way to obtain accurate estimates of ET over large areas (Irmak et al., 2012; Li et al., 2009; Glenn et al., 2007). The RS-based evapotranspiration algorithms utilize visible/near-infrared and thermal spectral measurements in energy balance models, empirical/statistical methods between ET and biophysical variables, vegetation indices or the surface temperature and trapezoid or triangle feature space methods (Glenn et al., 2007; Biggs et al., 2015; Hu et al., 2015). The remote sensing data can be obtained from numerous satellite sensors, including Landsat, Moderate Resolution Imaging Spectroradiometer (MODIS), Advanced Spaceborne Thermal Emission and Reflection Radiometer (ASTER) and NOAA-Advanced Very High Resolution Radiometer (AVHRR), all of which have different spatial, temporal and spectral characteristics.

High spatial resolution satellite imagery, like Landsat or ASTER, can be used to estimate ET at field scale (30 m), but have low temporal resolution (16 days). On the other hand, MODIS imagery have high temporal resolution (1 day), but moderate spatial resolution (250 m to 1 km). In most cases, at pixel scale of 1 km there is variability in land surface characteristics. Since ET is highly variable over heterogeneous surfaces, an important question arises as to whether the ET flux estimated from satellite imagery with such pixel resolution can be accurately represented.

In recent years, several global ET datasets were made available based on operational satellite products. These datasets differ in terms of forcing data, governing equations, spatial and temporal resolution (Hu et al., 2015). Among these datasets, the most widely used in hydrological and ecological studies is the MODIS Global Terrestrial Evapotranspiration Product (MOD16) which uses as inputs MODIS land cover, leaf area index (LAI) and albedo products, and global meteorological reanalysis data generated by the Global Modeling and Assimilation Office (GMAO) (Yang et al., 2015; Mu et al., 2009).

A very important issue when using operational satellite products is the accuracy assessment of these products. This process is called "validation". The validation of MOD16 ET product is an on-going activity by several researchers who explore the accuracy of the estimated ET across a range of land-cover types around the world. In most cases, the validation of MOD16 ET is performed against ground-based eddy covariance (EC) measurements of latent heat flux (LE). This approach may provide accurate results on a point/local scale, although the spatial resolution of the satellite-based products has a great influence on the validation of surface heat fluxes (Su et al., 1999; McCabe and Wood, 2006). In particular, the validation of coarse resolution products (e.g. MOD16 product with 1 km resolution) is very difficult due to the additional uncertainty introduced by the scale discrepancy between ground measurements and the satellite-based imagery (Ershadi et al., 2013; Hong et al., 2009). On a regional scale the complexity of ET process across heterogeneous land surface in conjunction with the coarse resolution of the MOD16 ET product requires a different validation approach.

In an attempt to overcome the above mentioned problems a number of studies suggested the use of aggregated fine resolution imagery (e.g Landsat) for the validation of coarse resolution products (McCabe and Wood, 2006; Ershadi et al., 2013; Liang et al., 2002; Hong et al., 2009). The fine resolution imagery with estimates of surface heat flux are first validated against ground-based measurements at a point scale and then aggregated to a lower spatial resolution, same as the product to be validated. In this way the coarse resolution product can be validated at a regional scale.

1.4 Objectives

The aim of this study is the validation of the MODIS 8-day ET composite (MOD16A2) over an agricultural area in Austria, namely the Marchfeld region, for a period of four months during the growing season of 2014.

The validation is performed at a regional scale, with a pixel-by-pixel comparison against ET maps aggregated at the same spatial and temporal resolution as the 8-day MOD16 ET product. These maps were previously validated at a point scale using eddy covariance data. The ET maps were created with the application of a model suitable for agricultural areas, the FAO-56 Penman-Monteith method with the use of high resolution Landsat-8 images.

In the context of this thesis and as part of the validation procedure followed, a series of tasks were performed that would give answers to the following specific research questions:

1) Regional ET maps were created from the implementation of the FAO-56 Penman-Monteith method with Landsat-8 images and standard meteorological data. How accurate are the ET estimations from these maps when compared against EC measurements?

2) For the aggregation of ET maps from fine (30 m) to coarse resolution (1 km) three different spatial aggregation methods were examined. Which spatial aggregation method provided better match?

3) How accurate are the remotely sensed and meteorological input data to the MOD16 algorithm?

4) What is the impact of LAI and soil water availability on MOD16 ET product?

5) How well the MOD16 ET product performs over the Marchfeld region?

2 Remotely sensed evapotranspiration

The first part of this chapter provides a brief review of the remote sensing-based methods for ET estimation. The second part of the chapter deals with the algorithms of the two RS-based methods used in the context of the thesis, the MOD16 algorithm and the FAO56 Penman-Monteith (FAO56-PM) "one-step approach" with satellite data. A detailed description of the theoretical background and the algorithm formulation of each RS-based method is given.

2.1 Methods to estimate ET from remotely sensed (RS) data

Biggs et al. (2015) group the available methods for estimation of ET from remotely sensed data in the following three basic families: 1) vegetation-based methods, 2) radiometric land surface temperature (T_s)-based methods and 3) radiometric land surface temperature (T_s)/vegetation index (VI) scatterplot methods.

Vegetation-based methods

Estimation of ET over a landscape with vegetation-based methods is an indirect approach that depends on vegetation indices (VIs) or related products from the reflectance of visible and near infrared (NIR) light from the canopy. VIs are highly correlated with plant physiological processes that depend on light absorption by a canopy such as ET and photosynthesis (Glenn et al., 2010, 2011; Kalma et al., 2008). VIs are an integrated product of Leaf Area Index (LAI), chlorophyll content, leaf angles, fractional cover and canopy architecture over vegetated surfaces (Nagler et al., 2004; Glenn et al., 2007). The vegetation-based methods may provide good results in arid or semiarid, fully vegetated surfaces where the dominant process is the transpiration (T) by plants. Vegation-based methods have been extensively applied in cropland areas for the estimation of crop evapotranspiration (ET_c), since VIs from satellite images can "represent" the crop development. An extended review on the vegetation-based methods for ET estimation can be found on Glenn et al. (2010) and Glenn et al. (2011).

Radiometric land surface temperature-based methods

Radiometric land surface temperature (T_s) methods are driven by a physical property of the surface, the radiometric land surface temperature (T_s), which is directly related to latent heat flux since the change of state of water from liquid to vapour uses energy in the environment that reduces the land surface temperature (Su et al., 2005). In the literature these methods are often called surface energy balance methods, since they solve the surface energy balance equation using the land surface temperature (T_s) to partition the available energy between the sensible (H) and latent heat fluxes (LE). An extended review on the various surface energy balance models can be found on Gowda et al. (2008) and Kalma et al. (2008).

T_s/VI scatterplot methods

The T_s/VI scatterplot, also called triangle or trapezoidal, methods are based on information derived from the "scatterplot" relationships between satellite derived vegetation indices (VIs) and radiometric land surface temperature (T_s) measures. An extended review on the T_s/VI scatterplot methods can be found on Petropoulos et al. (2009).

2.2 RS algorithms and products used in thesis

2.2.1 Estimation of ET with FAO56-PM method using RS data

Extended research on estimation of ET in agricultural areas for practical and operational management led to the development of the crop factor methods. The main assumption behind these methods is that ET can be estimated by two factors, one related with weather conditions and another one related with crop characteristics and crop management. The Food and Agriculture Organisation (FAO) Irrigation and Drainage Paper No. 56 (Allen et al., 1998) further extended this concept and proposed practical guidelines for computing crop evapotranspiration (ET_c) and crop water requirements in agricultural areas.

The FAO-56 paper represents ET as the product of two parameters: a) the reference evapotranspiration (ET_o) which takes atmospheric and climatic conditions into account and b) a crop coefficient representing the specific characteristics of the crop (Kc):

$$ET_c = Kc \cdot ET_o \tag{2.1}$$

Crop evapotranspiration under standard conditions (ET_c) is the actual evapotranspiration rate from disease-free, well-fertilized crops, grown in large fields, under optimum soil water conditions, and achieving full production under the given climatic conditions. ET_o is the theoretical evapotranspiration rate from a reference surface, not short of water. The reference surface is a hypothetical grass reference crop with specific characteristics (h_c=0.12 m, LAI=2.88 and albedo=0.23). The calculation of ET_o is performed with the Penman-Monteith equation using the previously mentioned canopy values for the hypothetical grass reference crop and for this reason the method is generally referred as FAO-56 Penman-Monteith (FAO56-PM). The single crop coefficient (Kc) is an empirical parameter that incorporates the effect of crop transpiration and soil evaporation. In the FAO56-PM approach it represents an integration of the effects of major characteristics that distinguish the crop from the reference crop ET_o. These characteristics are biophysical parameters related to: a) crop height (h_c) that affects roughness and aerodynamic resistance, b) crop-soil surface resistance which is affected by LAI, leaf condition, soil wetness and c) albedo of the crop-soil surface, which is affected by the fraction of ground covered by vegetation and by the soil surface wetness (Allen, 2000; Allen et al., 1998). The FAO56-PM methodology has been widely used throughout the world and nowadays is considered the standard method for reference evapotranspiration (ET_o)(Pereira et al., 2014).

In most RS-based applications of the FAO56-PM method the crop coefficient (Kc) is substituted by a VI derived from remotely sensed reflectance data in the visible and near-infrared spectral domains (Neale et al., 1989; Glenn et al., 2011). The reference evapotranspiration ET_o is calculated with the necessary meteorological data and then multiplied with the pixel based K_c for the calculation of ET_c at pixel level. An alternative conceptualization has been developed by D'Urso (2001) for the direct calculation of ET_c using the Penman-Monteith equation as introduced in the FAO-56 paper without the need of a crop coefficient. This methodology is called the "one-step approach" (Equation 2.2) and can be used for the direct estimation of ET_c (mm d^{-1} or mm h^{-1}) under standard conditions (disease-free, adequate fertilization and soil water availability) requiring as inputs standard meteorological data and crop specific biophysical parameters retrieved through remote sensing (Vuolo et al., 2015).

$$ET_c = f\{r, LAI, h_c | T_a, RH, S, U\} \tag{2.2}$$

where r is the albedo, LAI is the leaf area index, h_c is the crop height, T_a is air temperature, RH is the relative humidity and U is the wind speed.

The calculation of ET_c is achieved with the application of the Penman-Monteith equation (Equation 2.3) for the actual field conditions with crop biophysical parameters derived from remote sensing and standard meteorological data.

$$ET_c = \frac{86400}{\lambda}\left[\frac{\Delta\,(R_n - G)\; + \rho\, c_p\,(e_s - e_a)\, C_a}{\Delta + \gamma\,(1 + C_a/C_s)}\right] \tag{2.3}$$

where ET_c is the crop evapotranspiration (mm d^{-1}) or (mm h^{-1}), λ is the latent heat of vaporization of water (J kg^{-1}), Δ is the slope of the saturated vapour pressure-temperature curve $e_s(T_a)$, R_n is the net radiation flux density (W/m^2), G is the heat flux density into the soil (W/m^2), ρ is the air density (kg m^{-3}), c_p is the specific heat of dry air (J kg^{-1} K^{-1}), $e_s - e_a$ is the vapour pressure deficit at the given air temperature T_a(kPa), C_a is the aerodynamic conductance for heat transport (m s^{-1}), γ is the thermodynamic psychrometric constant(kPa K^{-1}), C_s is the canopy surface conductance (m s^{-1}).
The two conductance terms C_a, C_s are calculated as the inverse of the resistances defined by Allen et al. (1998):

$$C_a = \frac{k^2 U}{\ln\left(\frac{z_U - d}{z_{om}}\right)\ln\left(\frac{z_T - d}{z_{oh}}\right)} \tag{2.4}$$

$$\begin{aligned} C_s &= 0.005 LAI \quad \forall\, LAI \leq 4 \\ C_a &= 0.02 \quad \forall\, LAI > 4 \end{aligned} \tag{2.5}$$

where k is the von Karmans constant (0.41), z_U and z_T are respectively the measurement heights for wind speed and temperature, d is the zero-plane displacement height and the variables z_{om}, z_{om} represent the roughness lengths for momentum and heat, respectively, being estimated from canopy height h_c (Brutsaert, 1982). From the above equations it can be seen that C_a is a function of wind speed and canopy height. While, the surface conductance C_s depends on incoming solar radiation, vapour pressure deficit and soil water deficit (Vuolo et al., 2015).

If Equation 2.3 is applied a second time with the hypothetical parameters for the grass reference crop and the same climatic data as the first time, the reference evapotranspiration ET_o can be calculated. The ET_c/ET_o ratio calculated from the application of Equation 2.3 twice gives an analytical crop coefficient (Kc). This ratio is also called "evaporative fraction" (EF) at the satellite overpass and it is generally presumed constant, in between satellite overpasses, and with time of day (Allen, 2000).

The above methodology ("one-step approach") doesn't make distinction on the conductance terms related to soil evaporation and plant transpiration, thus considers the canopy as a "big-leaf", with a surface area expressed by LAI, crop height and albedo (r).

2.2.2 MOD16 Evapotranspiration

The MODIS global evapotranspiration (MOD16) is an operational ET product for the global vegetated land areas available from the year 2000 until now. The MOD16 product includes actual evapotranspiration (ET), latent heat flux (LE), potential evapotranspiration (PET) and potential latent heat flux (PLE) datasets at 1 km spatial resolution, for 8-day, monthly and annual intervals. These datasets are produced using the MOD16 ET algorithm by Mu et al. (2007, 2011) that is based on the work of Cleugh et al. (2007).

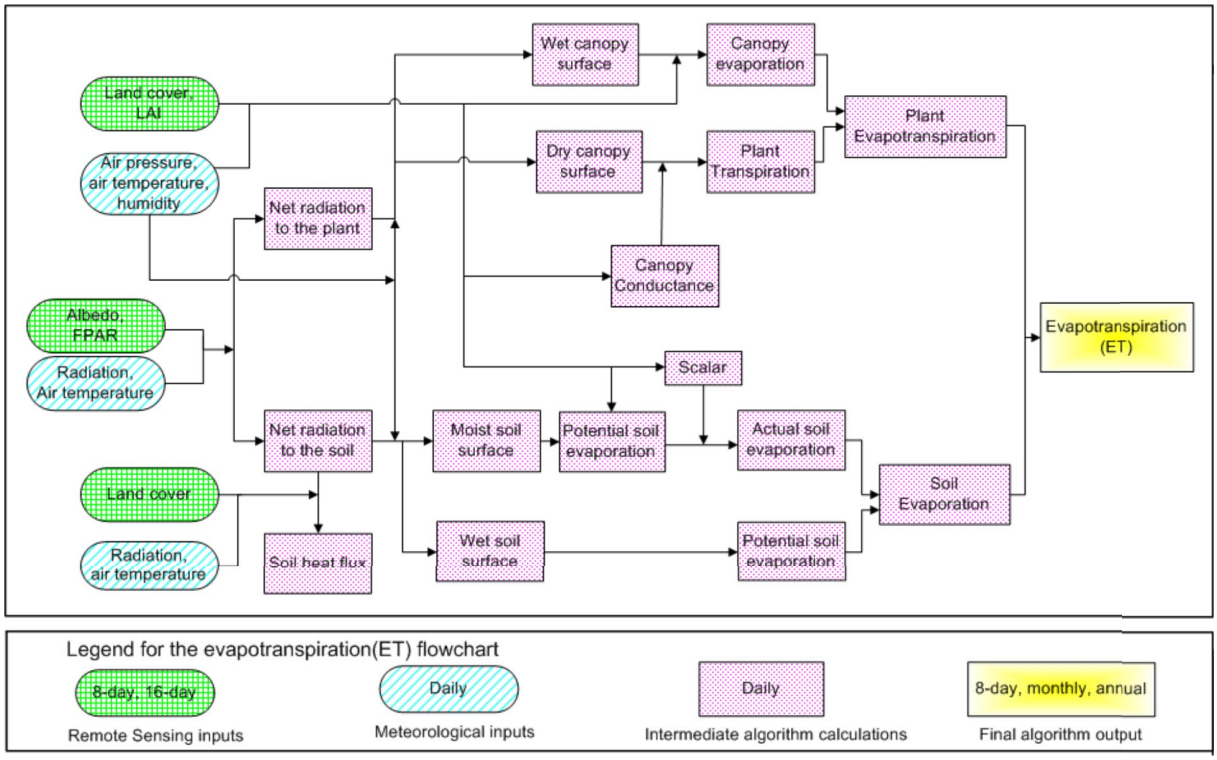

Figure 2.1: Flowchart of the MOD16 ET algorithm (Mu et al., 2011).

The MOD16 ET algorithm (or PM-Mu2011) is based on the Penman-Monteith equation and considers both the surface energy partitioning and atmospheric drivers on ET (Velpuri et al., 2013). It calculates ET using global meteorological data (daily air temperature, relative humidity, net radiation, wind speed) and remotely sensed Leaf Area Index (LAI), Vegetation Cover Fraction (F_C), albedo and land cover type.
The meteorological data used as inputs to the algorithm are the NASA's Global Modelling and Assimilation Office (GMAO) Modern-Era Retrospective Analysis for Research and Applications (MERRA) data. The remotely sensed inputs are the following MODIS data: 1) global 500 m^2 land cover from the MCD12Q1 product (yearly composite), 2) global 1 km^2 Leaf Area Index-Fraction of Photosynthetically Active Radiation (LAI/FPAR)from the MOD15A2 (8-day composite), 3) global 1 km^2 albedo (the 10th band of the White-Sky-Albedo) MCD43B3 (8-day composite).

Terrestrial ET includes evaporation from wet and moist soil, evaporation from rain water intercepted by the canopy before it reaches the ground, the sublimation of water vapour from ice and snow and the transpiration through stomata on plant leaves and stems. Therefore, the total evapotranspiration in MOD16 algorithm is calculated as the sum of soil evaporation E_s, interception evaporation E_i and canopy transpiration T_c (Equation 2.6). The daily ET is the sum of both daytime and nighttime ET.

$$ET = E_s + E_i + T_c \tag{2.6}$$

Each component of the total ET is formulated based on the Penman-Monteith equation:

$$ET = \frac{\Delta\, A + \rho\, C_p\, (e_s - e_a)/r_a}{\Delta + \gamma\, (1 + r_s/r_a)} \tag{2.7}$$

where ET is evapotranspiration, Δ is the slope of the curve relating saturated water vapour pressure to temperature, A is available energy partitioned between sensible heat, latent heat and soil heat fluxes on land surface, ρ is air density, C_p is the specific heat capacity of air, $(e_s - e_a)$ is vapour pressure deficit (VPD), r_a is the aerodynamic resistance and γ is the psychrometric constant. The term r_s is an effective resistance to evaporation from land-soil surface and transpiration from the plant canopy.

Net radiation

The net incoming solar radiation is calculated with the following equation:

$$R_n = (1 - \alpha)R_s + (\epsilon_a - \epsilon_s)\sigma(273.15 + T^4) \tag{2.8}$$

where α is the albedo from the 8-day MCD43B3 albedo (the 10th band of White-Sky-Albedo), R_s is the downward shortwave radiation, ϵ_a is the atmospheric emissivity, ϵ_s is the surface emissivity, σ is the Stefan-Boltzmann constant (= 5.67 10^{-8} W m^{-2} K^{-4}) and T_a is air temperature (°C). The net incoming solar radiation at night is assumed to be zero.

Vegetation cover fraction

Net radiation(R_n) is linearly partitioned between the canopy and the soil surface based on the 8-day 1-km^2 MODIS 15A2 FPAR (Fraction of Absorbed Photosynthetically Active Radiation), which is considered as a surrogate of vegetation cover fraction (F_c) (Los et al., 2000).

$$\begin{aligned} A &= R_n \\ A_c &= F_c \cdot A \\ A_s &= (1 - F_c) \cdot A - G \end{aligned} \tag{2.9}$$

where A is the available energy partitioned between sensible heat, latent heat and soil heat fluxes on land surface, A_c is the available energy for the canopy, A_s is the available energy for the soil surface and G is the soil heat flux.

Wet cover fraction

The MOD16 algorithm uses an empirical relationship developed by Fisher et al. (2008) to distinguish a wet surface from a dry surface. The surface can be either canopy or soil. The water cover fraction (F_{wet}) is formulated in the following way:

$$F_{wet} = \begin{cases} 0 & RH < 70\% \\ RH^4 & 70\% \leq RH \leq 100\% \end{cases} \tag{2.10}$$

where RH is relative humidity.

Evaporation from wet canopy

Precipitation interception or condensation of atmospheric vapour results in the presence of liquid water in the canopy. In this case evaporation from the wet canopy occurs, which is calculated in the MOD16 algorithm in the following way:

$$E_{C,wet} = \frac{\Big(\Delta A_c + \rho C_p VPD F_c / r_{awc}\Big) F_{wet}}{\Delta + (1 + r_{swc}/r_{awc})} \tag{2.11}$$

where r_{awc} and r_{swc} are the aerodynamic and wet canopy resistances of the wet canopy.

Transpiration from dry canopy

Vegetation transpiration occurs from a dry canopy surface and is mainly regulated by canopy conductance (canopy resistance) and aerodynamic conductance (aerodynamic resistance). The water source for transpiration is the root-zone soil moisture. Vegetation transpiration is calculated as:

$$T_{C,dry} = \frac{\Big(\Delta A_c + \rho C_p VPD F_c / r_{ac}\Big)\Big(1 - F_{wet}\Big)}{\Delta + \gamma(1 + r_{sc}/r_{awc})} \tag{2.12}$$

where r_{ac} and $r_{sc}$are the aerodynamic and canopy resistances of the dry canopy.

$$\begin{aligned} r_{sc} &= 1/C_C \\ C_C &= \frac{G_{S2}(G_S + G_{CU})}{G_{S2} + G_S + G_{CU}} LAI(1 - F_{wet}) \\ G_S &= C_L \cdot m(T_{min}) \cdot m(VPD) \cdot r_{corr} \end{aligned} \tag{2.13}$$

In the MOD16 algorithm stomatal conductance (G_S) is mainly affected by the minimum air temperature and VPD. r_{corr} is a correction coefficient for the maximum stomatal conductance accounting for the influence of atmospheric pressure and temperature. The parametrization of stomatal conductance is based on C_L, which is the mean potential stomatal conductance per unit leaf area. It's set differently for different biomes and the corresponding values are listed in a Biome-Property-Look-Up-Table (BPLUT) in Mu et al. (2011). Finally, LAI is used to scale stomatal conductance (G_S) from the leaf level to a canopy level, as a canopy conductance (C_C).

Evaporation from wet soil surface

The evaporation from a wet soil surface (saturated) is considered as potential evaporation and is calculated in the following way:

$$E_{S,wet} = \frac{\Big(\Delta A_s + \rho C_p VPD(1 - F_c)/r_{as}\Big)F_{wet}}{\Delta + (1 + r_{ss}/r_{as})} \tag{2.14}$$

where r_{as} is the aerodynamic resistance of the soil surface and r_{ss} is the sum of the surface resistance and the aerodynamic resistance for vapour transport.

Evaporation from dry soil surface

Evaporation for a dry soil surface is mainly constrained by the soil surface moisture (Di et al., 2015). The potential evaporation rate is corrected by an empirical soil moisture constraint function of VPD and RH as in the Fisher et al. (2008) ET model.

$$E_{S,dry} = \frac{\Big(\Delta A_s + \rho C_p VPD(1 - F_c)/r_{as}\Big)\Big(1 - F_{wet}\Big)}{\Delta + (1 + r_{ss}/r_{as})} \Big(\frac{RH}{100}\Big)^{VPD/200} \tag{2.15}$$

Total daily ET

The total daily ET is:

$$ET = E_{C,wet} + T_{C,dry} + E_{S,dry} + E_{S,wet} \tag{2.16}$$

2.3 Literature review on MOD16 validation studies

This section provides an overview of research studies related with the validation of MOD16 ET product in many regions of the world and at various temporal scales. The majority of these validation studies is performed against ET measurements from Eddy Covariance (EC) towers.

Mu et al. (2011) performed an evaluation of the daily ET estimates from MOD16 against measured ET at 46 AmeriFlux EC towers located in North America over the years 2000 to 2006. The 46 EC towers covered a wide range of climates and land cover types. The mean absolute error (MAE) of daily ET between MOD16 and EC measurements was 0.31 mm/day, the daily root-mean-square error (RMSE) 0.90 mm/day and the average correlation coefficient (R) had a value of 0.58. Kim et al. (2012) evaluated the 8-day MOD16 ET product at 17 EC flux tower sites in Asia over a period of 7 years from 2000-2006. The sites of the EC towers were in a range of climatic conditions and the majority (13 sites) were located in forested areas while the rest in croplands (2 sites) and grasslands (2 sites). Best performances of the MOD16 estimated ET were observed at forest sites, while poor performance was found at sites with arid and polar climates. Tang et al. (2015) evaluated the 8-day MOD16 ET product against EC and large aperture scintillometer (LAS) measurements at seven sites in North and Northwest China from 2008 to 2011. The seven sites represented a wide range of climatic conditions and most of them were located in croplands. They found that the 8-day MOD16 ET satisfactory reproduced the temporal pattern of ET for both LAS and EC measurements at all seven sites. The relative bias and the relative RMSE varied between 5% and -59% and between 35% and 120%, respectively, for the EC validation. For the LAS validation the relative bias and the relative RMSE varied between 6% and -69% and between 55% and 108%, respectively. Ramoelo et al. (2014) evaluated the 8-day MOD16 ET product using data from two EC towers in South African savanna ecosystems over a period of 11 years from 2000 to 2010. They found that MOD16 ET underestimated ET with errors ranging from 2-7 mm/8day at the one site and approximately 3 mm/8day at the second site. Hu et al. (2015) evaluated the 8-day MOD16 ET product across a wide range of ecosystems and climates at 15 EC towers in Europe for the year 2011. The MOD16 ET product performed best for cropland and grassland sites located in temperate and fully humid climate with average correlation coefficients (R) of 0.90 and 0.93 and RMSE of 0.6 mm/day and 0.57 mm/day, respectively. The worst performance of the MOD16 ET was observed for shrublands located in semi-arid climate with average correlation coefficients (R) of 0.35 and RMSE of 0.36 mm/day. In the forest sites high average correlation coefficients (R) were found ranging from 0.45 to 0.98 and RMSE values from 0.34 to 1.57 mm/day. In most forest sites ET was overestimated during summer by an average value of 0.5 mm/day.

Some recent studies further extended the validation of MOD16 ET product not only at point scale but also on a regional/basin scale. Velpuri et al. (2013) evaluated the monthly MOD16 ET product (a) at a point scale using measurements from 60 FLUXNET EC towers over the conterminous United States (CONUS) and (b) at basin scale using gridded FLUXNET data which are compiled by upscaled EC measurements of the FLUXNET project. The point scale validation over the years 2001-2007 revealed that the accuracy of MOD16 ET was highly variable with land cover and climatic conditions. The MOD16 ET product performed better in cropland and woody savanna land cover types, with R^2 of 0.70 and 0.71, respectively, and RMSE of 19 mm/month and 25 mm/month, respectively. The worst results were observed in grassland and forest land cover types, with R^2 of 0.41 and 0.56, respectively, and RMSE of 29 mm/month and 33 mm/month, respectively. Basin scale validation of the MOD16 ET product indicated that MOD16 matched the accuracies of the global gridded FLUXNET ET dataset at different scales, having also low levels of uncertainty (13-18% of annual estimates). These results illustrated the reliability of monthly MOD16 ET product for basin scale ET estimation.

3 Material and methods

3.1 Study area

The study area is the Marchfeld region, an agricultural area in Lower Austria located in the very East of Austria (Lat N 48°12 , Long E 16°34). Marchfeld region has an area of approximately 1000 km^2 and is part of the the greater "Vienna Basin" (Figure 3.1). The study site is considered among the most important crop production regions in Austria (Kirchner and Schmid, 2013).

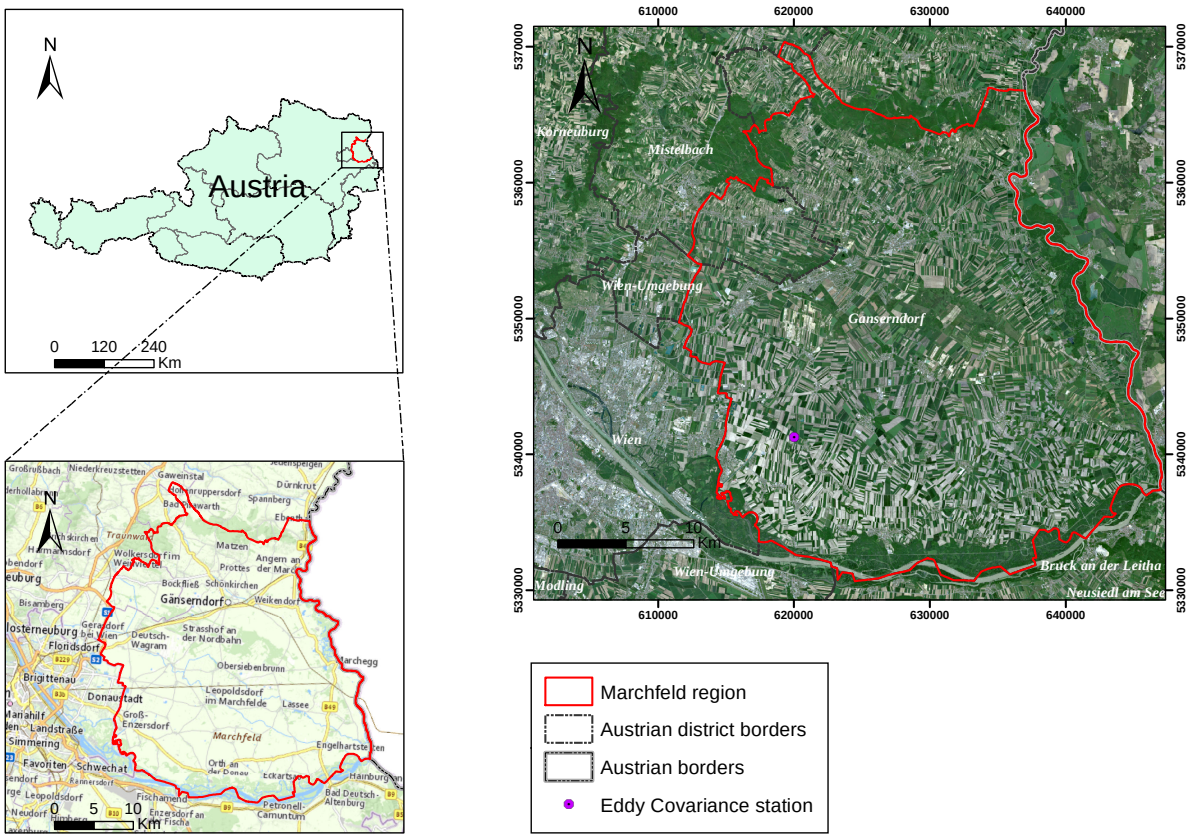

Figure 3.1: Overview of the study area. The upper left map depicts the location of Marchfeld region in Austria. The bottom left map shows the boundaries of the study area overlaid on top of a topographic map. The center map illustrates the boundaries of the study area overlaid on top of an orthophoto basemap (http://www.basemap.at/). In the center map the location of the EC station (purple dot) is also shown.

3.1.1 Climate

The Marchfeld region is located at the western end of the Pannonian climate-region and is characterized by semi-arid climatic conditions. The topography of the area is flat, with elevations ranging from 137 m to 165 m above sea-level. Based on measurements during 1971-2000 from the weather station Groß-Enzersdorf (ZAMG), located in the South-West of Marchfeld region, the average annual temperature is 9.8°, the average annual precipitation 520 mm and the mean duration of sunshine around 1900 hours per year (Figure 3.2). The amount of precipitation accounted for the growing season only (April-September) is around 320 mm and in conjunction with the strong winds occurring in the area result in dry climatic conditions (Vuolo et al., 2015; Neugebauer, 2013).

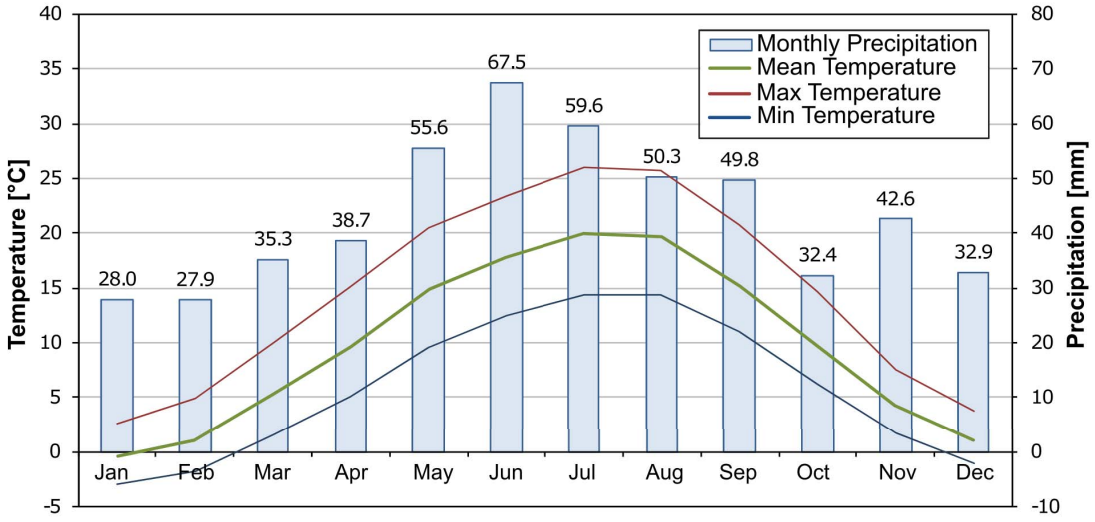

Figure 3.2: Mean monthly temperature and precipitation from the weather station Groß-Enzersdorf (ZAMG) during the period 1971 to 2000 (Freyer et al., 2010). Also plotted in the chart are the monthly maximum (red line) and minimum (blue line) temperatures for the period 1971-2000.

The following climate chart (Figure 3.3) illustrates the monthly measurements of year 2014 from the weather station Groß-Enzersdorf (ZAMG).

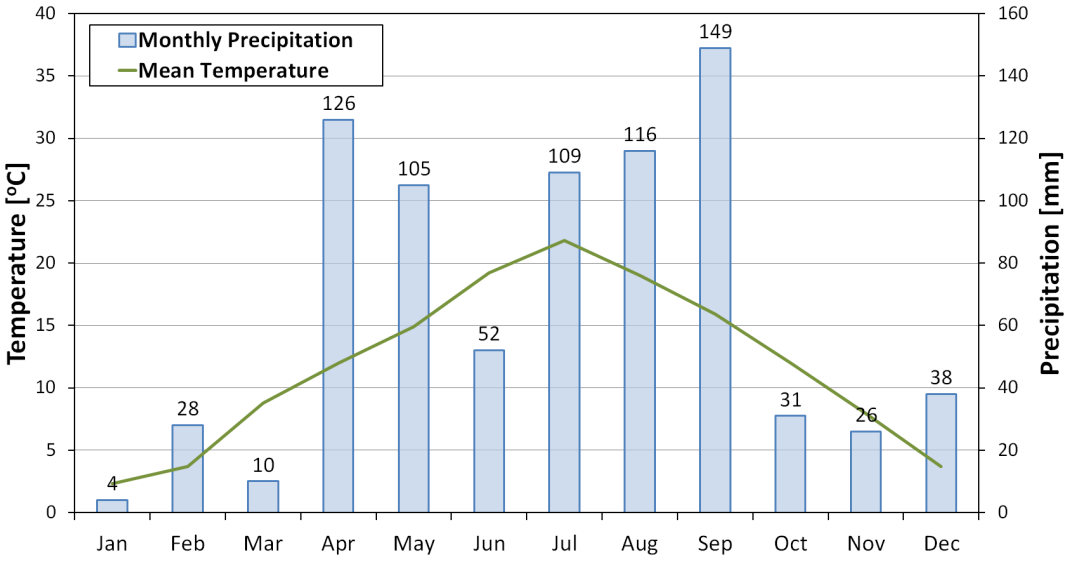

Figure 3.3: Monthly mean temperature and total precipitation from the weather station Groß-Enzersdorf (ZAMG) for the year 2014.

3.1.2 Agricultural activity in Marchfeld

Based on the Food and Argiculture Organization (FAO) World Soil Classification the dominant soil types in the area are Chermozen and Fluvisol. The general soil conditions of Marchfeld are characterized by a humus-rich A horizon and a sandy C horizon, followed by fluvial gravel from the former river bed of the Danube river (Richter et al., 2008). The cropland area covers about 60,000 ha of the Marchfeld region, with the major crops being vegetables (11%), sugar beet (10%) and potatoes (7%) (Neugebauer, 2013). Apart from the dry climate, another limiting factor for agricultural production is the low field capacity of 70 mm or less which results in low soil water capacity (Neugebauer, 2013). Due to these reasons irrigation techniques are applied to approximately 21,000 ha (30% of the cropland area) in order to supply water for the demanding agricultural activity (Vuolo et al., 2015).

3.2 Data

3.2.1 Remotely sensed (RS) data

Landsat data

Four Landsat-8 scenes over the Marchfeld region were acquired between May and September of 2014, covering a time period of 113 days. The selection of the four scenes was based on the following two criteria: a) the scenes should represent different stages of the crop development during the growing season of 2014 at the Marchfeld region and b) the scenes should have minimum or no cloud coverage over the Marchfeld region. The images were available from United States Geological Survey (USGS) EarthExplorer website – earthexplorer.usgs.gov).

Landsat-8 carries two sensors, the Operational Land Imager (OLI) and the Thermal Infrared Sensor (TIR), providing images every 16 days. The OLI sensor collects image data from 9 shortwave spectral bands with 30 m spatial resolution for all bands except the panchromatic (15 m). The TIR sensor collects image data for the two thermal bands with 100 m spatial resolution (resampled to 30 m for Level 1 products).

Further details for the Landsat scenes used in the study are given in Table 3.1.

Table 3.1: Information on acquired Landsat 8 imagery used in this thesis.

No.	Satellite	Sensor	Acquisition date	DOY	Scene Path/Row	Cloud cover (%)
1	Landsat 8	OLI	20 May 2014	140	190/26	0.59
2	Landsat 8	OLI	7 July 2014	188	190/26	3.85
3	Landsat 8	OLI	8 August 2014	220	190/26	14.43
4	Landsat 8	OLI	9 September 2014	252	190/26	51.37

MODIS data

The MODerate Resolution Imaging Spectroradiometer (MODIS) instruments on-board NASA's Terra and Aqua satellites are multispectral imaging radiometers with 36 spectral bands from approximately 0.4 to 14.0 µm. The spatial resolution of the MODIS instruments varies with spectral band, and ranges from 250 m to 1 km at nadir. MODIS provides daily global observations that are used in a wide range of products for land, ocean and atmospheric properties.
The MODIS global evapotranspiration product (MOD16) can be obtained from the University of Montana's Numerical Terradynamic Simulation Group website (ftp://ftp.ntsg.umt.edu/pub/MODIS/NTSG_Products/MOD16/). For the purpose of this study the MOD16A2 8-day composite at 1 km spatial resolution was obtained, among the available datasets from the MOD16 product. In total 12 MOD16A2 8-day composites were

downloaded for the time period from the 25th of May 2014 (DOY 145) to the 28th of August 2014 (DOY 240). Each composite is named with the first Julian date of the year (DOY) of the 8-day time period it represents. Consequently for our case, the first composite representing the time period from 25/5/2014 to 1/6/2014 is named "DOY 145" and the last composite representing the time period from 21/8/2014 to 28/8/2014 is named "DOY 233". The same format of names are used through the rest of the thesis.

The MOD16A2 product includes five layers with the following specifications:

i) The 8-day ET and PET layers are the sum of ET and PET, respectively, during the following 8-day time period (mm/8day).
ii) The 8-day LE and PLE layers are the average 8-day latent heat flux and potential latent heat flux, respectively, during the following 8-day time period (10^{-4}J/m^2/day).
iii) The ET_QC layer is the quality control of the MOD16A2 product, inherited form the MODIS LAI product MOD15A2 in the same period.

In addition to the MOD16A2 product, the MODIS products used as inputs to the MOD16 algorithm were also acquired from NASA's Land Processes Distributed Active Archive Centre (https://lpdaac.usgs.gov/data_access/data_pool/) for the time period from 17/5/2014 (DOY 137) to 28/8/2014 (DOY 240). In the case of MODIS Land Cover MCD12Q1 product, which is a yearly composite, the latest available product for download was for year 2012. It is assumed that the land cover of the area hasn't changed since 2012.

A list with all the MODIS products acquired and further details on each of them can be found in Table 3.2.

Table 3.2: List of MODIS products used in this thesis.

MODIS product	Layer	Spatial res.	Temporal res.	DOY (2014)
MOD16A2	ET	1 km	8-day	145 - 233
MOD15A2	LAI	1 km	8-day	137 - 233
MCD43B3	Albedo (Band 10-WSA)	1 km	8-day	137 - 233
MCD12Q1	LC Type 2	500 m	Yearly	-

MERRA-GMAO data

The MOD16 algorithm computes ET at a daily time step using meteorological data from the gridded dataset Modern Era Retrospective Analysis for Research and Applications (MERRA) provided by the NASA Global Modelling Assimilation Office (GMAO). MERRA is a NASA reanalysis dataset generated using the Goddard Earth Observing System Model (GEOS-5) Atmospheric Data Assimilation System (ADAS)(Lucchesi, 2012). Reanalysis combine model fields with observations distributed irregularly in space and time into a spatially complete gridded meteorological data set, with an unchanging model and analysis system spanning the historical data record (Rienecker et al., 2011). Further details regarding the MERRA system can be found in Rienecker et al. (2011) and information regarding the gridded output files produced by MERRA reanalysis can be found in Lucchesi (2012).

The MERRA data are available through the Goddard Earth Sciences (GES) Data and Information Services Center (DISC) website (http://disc.sci.gsfc.nasa.gov/mdisc/). For the purpose of this thesis data from two MERRA-GMAO collections were acquired for a spatial region covering the entire study area, for the year 2014. From the *MERRA IAU 2d surface and TOA radiation fluxes (tavg1_2d_rad_Nx)* collection, the following products were extracted: a) Surface net downward shortwave flux (SWGNT,W/m^2) and b) Surface net downward longwave flux (LWGNT,W/m^2). From the *MERRA IAU 2d atmospheric single-level*

diagnostics (tavg1_2d_slv_Nx) collection, the following products were extracted: a) Temperature at 2 m above the displacement height (T2M,K) and b) Specific humidity at 2 m above the displacement height (QV2M,kg kg^{-1}). The extracted data products have spatial resolution of 1/2 °×2/3° in latitude/longitude and temporal resolution of 1 hour.

The above gridded MERRA-GMAO data products were downscaled to the spatial resolution of MODIS data (1 km) using bilinear interpolation and were also reprojected to the geographic projection of MODIS data. The MERRA-GMAO meteorological data used in the MOD16 algorithm are downscaled to MODIS resolution using a non-linear interpolation (Zhao et al., 2005; Mu et al., 2011).

3.2.2 Ground-based data

Eddy Covariance (EC) measurements

Eddy Covariance (EC) stations measure turbulent fluxes of sensible (H) and latent heat (LE) at a point/local scale through the eddy covariance technique, which measures the covariance of the heat and moisture fluxes, respectively, with vertical velocity using rapid response sensors at frequencies typically equal to 20 Hz (Wang and Dickinson, 2012). Although EC measurements are labour intensive and time consuming, they are considered the best and most accurate method to measure sensible (H) and latent heat (LE) fluxes and they are regularly used in validation studies of ET estimates from different models and methods (Wang and Dickinson, 2012; Verstraeten et al., 2008).

Sensible (H) and latent heat (LE) flux measurements from an EC station located in the Marchfeld region (Figure 3.1) were available for the time period between 24/5/2014 (DOY 144) and 31/8/2014 (DOY 243). The fluxes were calculated every 15-min and they were aggregated to hourly (60-min) intervals for the validation procedure. The aggregated hourly measurements were considered valid only when there were at least three 15-min observations at each hour. The hourly measured latent heat flux (LE,W/m^2) at the EC station was converted to ET (mm/h) with the following equation:

$$ET = \frac{LE}{\lambda} \tag{3.1}$$

where λ is the latent heat of vaporization (2.45 MJ/kg).

The EC station also included a net radiometer that measured the net radiation (R_n,W/m^2) and soil heat flux plates that measured the ground heat flux (G,W/m^2). Figure 3.4 shows the energy balance closure between the measured $R_n - G$ (available energy) and the measured $H + LE$ (turbulent fluxes) values for valid hourly (60-min) periods. Also, the exact location of the EC station, which was installed in a maize field, is shown in Figure 3.4.

In addition to the EC station, other ancillary data such as incoming short-wave radiation, air temperature, rainfall , relative humidity and wind speed were available from a nearby weather station at the BOKU Experimental Farm in Groß-Enzersdorf. Also, the volumetric soil water content measurements at 5, 10, 30, 50 and 70 cm depths from a CS616 Water Content Reflectometer (Campbell Scientific Inc.) were available. All the data were available at hourly intervals for the same time period as the EC data, namely between 24/5/2014 (DOY 144) and 31/8/2014 (DOY 243). For some calculations and some comparisons the hourly measurements were aggregated to daily and 8-day sums or daily and 8-day averages, depending on the situation.

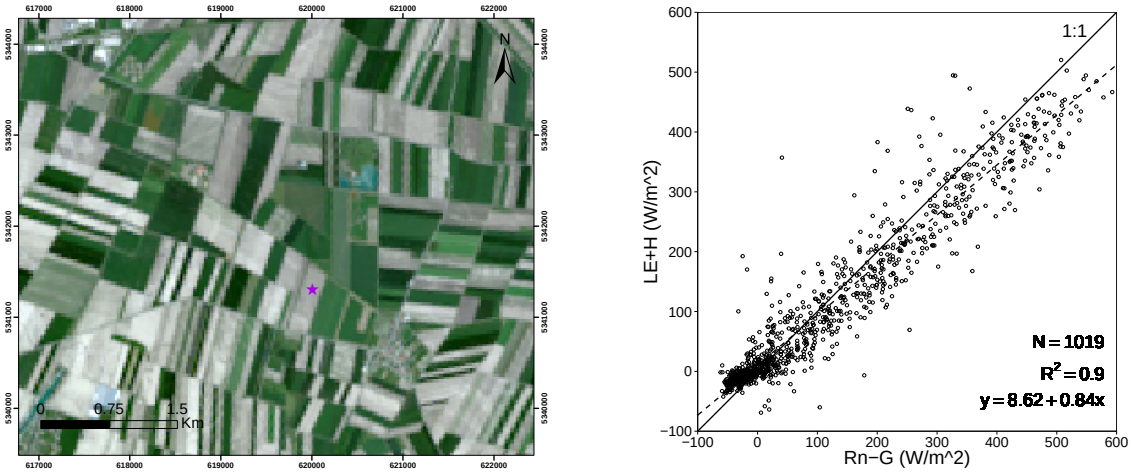

Figure 3.4: Left: Exact location of the EC station in a maize field, shown with a purple star. Right: Surface energy balance closure at the EC station based on valid 60-min fluxes of sensible (H) and latent heat (LE), net radiation (Rn) and ground heat flux (G) measurements.

3.3 Data processing

For the application of the FAO56-PM "one-step approach" method, as explained in Section 2.2.1, from each Landsat-8 image the LAI, albedo (r) and crop height (h_c) maps need to be derived.

Firstly, a subset of the Landsat scenes was selected that covered the entire Marchfeld region. Afterwards, an atmospheric correction was performed to the subset of the Landsat-8 scene with the ATCOR-2 module of ERDAS Imagine commercial software package (Geosystem Gmbh, 2014), in order to remove the effects of diffusion and scattering by atmosphere on the reflectance values of the imagery. ATCOR-2 is based on the MODerate resolution atmospheric TRANsmission (MODTRAN version 4) model and uses look-up-tables with pre-calculated model simulations for different satellite sensor types and a range of atmospheric conditions (Liang et al., 2001; Richter, 1998, 1996).

The albedo (r) was extracted as part of the value-added products from ATCOR-2 after the atmospheric correction (Vanino et al., 2015; Richter, 2001).

The LAI was derived from the surface reflectance with the application of Clevers' Leaf Area Index by Reflectance (CLAIR) model (Clevers, 1989). The CLAIR model is based on the Weighted Difference Vegetation Index (WDVI), which is a radiometric index calculated as:

$$WDVI = \rho_{NIR} - \rho_{red}\frac{\rho_{s,NIR}}{\rho_{s,red}} \tag{3.2}$$

where ρ_{NIR} is the reflectance of the NIR band, ρ_{red} is the reflectance of the red band and $\rho_{s,NIR}$ is the NIR reflectance of the soil and $\rho_{s,red}$ is the red reflectance of the soil. The ratio of NIR and red soil reflectance is known as "soil line slope".

The LAI is related to the WDVI with the following expression:

$$LAI = -\frac{1}{\alpha}\ln\left(1 - \frac{WDVI}{WDVI}\right) \tag{3.3}$$

where α is an empirical parameter depending on canopy structure and $WDVI$ is an asymptotical limiting value for WDVI at very high LAI values.

An extended review on the derivation of crop-specific biophysical parameters from satellite imagery for the application of the FAO56-PM "one-step approach" can be found in D'Urso et al. (2010) and Vuolo et al. (2015).

The MODIS products are provided in the Earth Observing System-Hierarchical Data Format (EOS-HDF) and in Sinusoidal Projection. To perform the comparisons between MODIS and Landata data a number of pre-processing procedures need to be followed. All the acquired MODIS products were reprojected to 1 km spatial resolution and a subset with the same spatial extent as with the Landsat imagery was extracted.

For the MERRA-GMAO extracted products the following calculations were performed to obtain the meteorological variables used in the MOD16 algorithm:

a) Net radiation (R_n,W/m^2) was calculated with the following formula:

$$R_n = SWGNT + LWGNT$$

where SWGNT is the surface net downward shortwave flux (W/m^2) and LWGNT is surface net downward longwave flux (W/m^2).

b) Relative humidity (RH,%) was calculated from specific humidity (QV2M,kg kg^{-1}) and air temperature (T2M,K) with the following formula:

$$RH = 0.263pQV2M \left[\exp\left(\frac{17.67(T2M - T_0)}{T2M - 29.65}\right)\right]^{-1}$$

where p is air pressure (1013.25 Pa) and T_0 is reference temperature (273.16 K).

c) Air temperature (T2M,K) was converted from Kelvin to Celsius.

3.4 Methodology

The study period for the validation of 8-day MOD16A2 product is limited to time period of available EC measurements, specifically between 24/5/2014 (DOY 144) and 28/8/2014 (DOY 240). The validation is performed through the following steps. Firstly, the hourly crop evapotranspiration (ET_c) was estimated by implementing the FAO56-PM "one-step approach" with Landsat-8 images and standard meteorological data. Secondly, the hourly ET_c estimations were validated against ET measurements from the EC station located in the study area. Afterwards, the hourly ET maps were spatially and temporally aggregated to match the MOD16 ET resolution. Finally, the validation of 8-day MOD16A2 product was performed with intercomparison against the validated ET maps from the FAO56-PM "one-step approach".

The flowchart in Figure 3.5 shows the computational steps followed in this thesis for the validation of the 8-day MOD16 ET product.

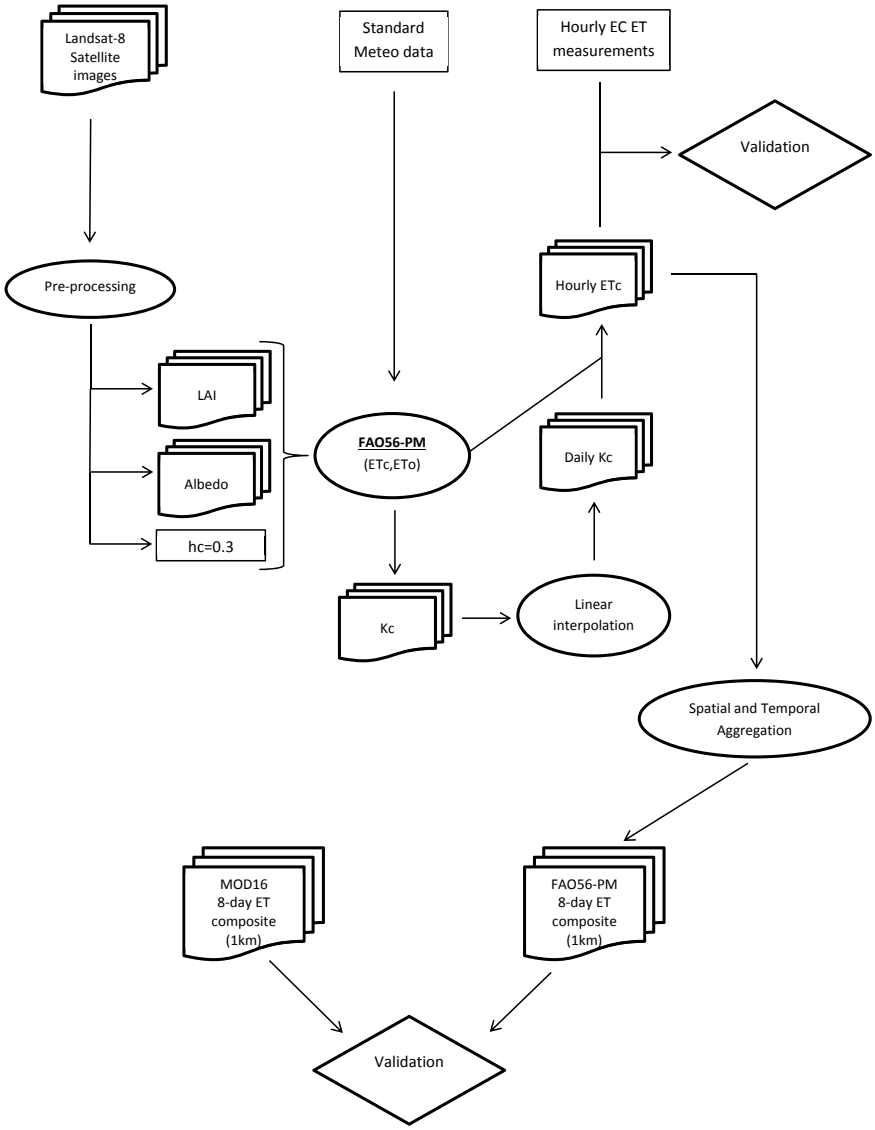

Figure 3.5: Flowchart of the methodology followed for the validation of 8-day MOD16 ET.

3.4.1 Application of FAO56-PM "one-step approach"

The application of FAO56-PM "one-step approach" for regional ET mapping at high spatial resolution was performed through the following steps. Firstly, Equation 2.3 was applied two times for the calculation of ET_o and ET_c at DOY 140, DOY 188, DOY 220 and DOY 252. The calculation of ET_c (mm/day) at these four DOYs was performed with the LAI and albedo maps derived from Landsat-8 images and the corresponding daily meteorological data from the Groß-Enzersdorf weather station (BOKU). The crop height (h_c) was assumed constant at 0.3 m for all calculations. The calculation of daily ET_o (mm/day) was achieved with the standard parameters for a reference crop (h_c=0.12 m, LAI=2.88 and albedo=0.23) and the same daily meteorological data used for ET_c. Afterwards, Equation 3.4 was applied and each of the four raster based ET_c maps was divided with the scalar ET_o of that DOY, resulting in raster based crop coefficient (Kc) maps for each of the four DOYs.

$$K_c = \frac{ET_c}{ET_o} \tag{3.4}$$

During the growing season the Kc values for most agricultural crops increase from a minimum value at the start of the growing season to a maximum value at full canopy. Kc decreases as the crop matures (Glenn et al., 2007). The theoretical temporal evolution of Kc during the crop development stages can be seen in Figure 3.6. Having calculated the raster based "analytical" Kc values for four stages of the crop development during the growing season of 2014 and under the assumption that Kc varies linearly between the end of a previous stage and the beginning of the next stage (Allen et al., 1998), the four Kc raster maps were interpolated to produce 113 daily Kc raster maps, spanning the period from DOY 140 to DOY 252.

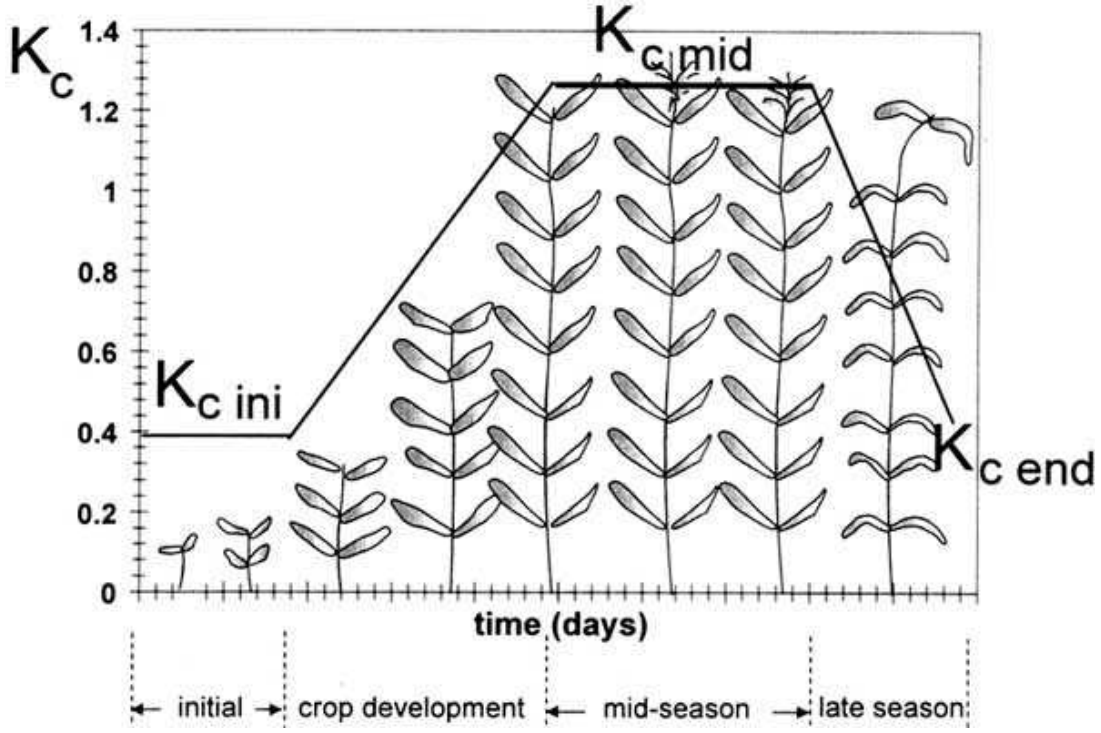

Figure 3.6: Theoretical crop coefficient (Kc) curve during crop growth (Allen et al., 1998).

Furthermore, the hourly reference evapotranspiration (ET_o,mm/hr) was calculated for the time period between 24/5/2014 (DOY 144) and 28/8/2014 (DOY 240) from the available hourly meteorological data at Groß-Enzersdorf weather station, applying the FAO56-PM equation (Equation 2.3) with the standard parameters for a reference crop (h_c=0.12 m, LAI=2.88 and albedo=0.23). The guidelines followed for the calculation of ET_o at hourly time step are documented in Allen et al. (1998).

Finally, the hourly crop evapotranspiration (ET_c,mm/hr) raster maps of Marchfeld region were calculated for the time period from 24/5/2015 (DOY 144) to 28/8/2014 (DOY 240) as the product of the hourly reference evapotranspiration (ET_o,mm/hr) by the daily Kc raster maps, which were assumed constant during the 24-hours of each day.

3.4.2 Point scale validation against EC measurements of ET

The hourly crop evapotranspiration (ET_c) raster maps were evaluated against ground-based EC measurements of evapotranspiration (ET_{EC}). Hourly time series were extracted from the crop evapotranspiration (ET_c) raster maps using a 1x1 pixel window and a 3x3 pixel window at the location of the EC station. In the 3x3 pixel window approach the average value of ET_c obtained from the 9 pixels was calculated.

The validation of the ET_c raster maps (hereafter called $ET_{RS,FAO56-PM}$) against EC measurements would justify their use as a gridded surrogate of observed ET at hourly time step and as the "ground-truth" for regional validation of the MOD16 ET product.

3.4.3 Aggregation of $ET_{RS,FAO56-PM}$

Temporal aggregation

Since the MOD16 ET products ($ET_{RS,MOD16}$) are 8-day composites, the same composites should be created for $ET_{RS,FAO56-PM}$. Firstly, the hourly $ET_{RS,FAO56-PM}$ raster maps were aggregated to a daily time step, where each pixel represented the sum of daily ET. This process resulted in 97 daily $ET_{RS,FAO56-PM}$ raster maps of the Marchfeld region, from DOY 144 to DOY 240. Afterwards, from the daily $ET_{RS,FAO56-PM}$ products, 8-day composites were derived to coincide with the $ET_{RS,MOD16}$ temporal scale. The 8-day composite represents the sum of ET over an 8-day time period and is named after the first DOY of the 8-day period, following the concept of all MODIS products and the $ET_{RS,MOD16}$. In total twelve $ET_{RS,FAO56-PM}$ 8-day composites were created (Table 4.3) for the time period from 25/5/2014 (DOY 145) to 28/8/2014 (DOY 240).

Spatial aggregation

The spatial resolution of the 8-day $ET_{RS,FAO56-PM}$ composites was 30 m, as they were derived from Landsat-8 images. The MOD16 ET products have 1 km spatial resolution inherited from the 1 km MODIS products used as inputs to the algorithm (MOD15A2, MCD43B3, MCD12Q1). To perform an intercomparison between the the two products at a pixel level they should have the same spatial resolution, namely the same pixel size. The process of obtaining coarse resolution products from fine resolution products is called spatial aggregation. During an aggregation process the original raster data are reduced to a smaller number of data units, namely pixels, covering the same spatial extent. Spatial aggregation is considered to modify the statistical and spatial characteristics of the original data, leading to loss of detail. The most "appropriate" aggregation method is the one that retains the statistical characteristics of the original data in the aggregated data (Bian and Butler, 1999).

Regarding the application of spatial aggregation techniques on satellite-based evapotranspiration models/products there are two approaches. In the first approach, called "input aggregation", the input forcings of the evapotranspiration model are first aggregated and then the model is applied. While in the second approach, called "flux aggregation", the estimated ET is aggregated after the application of a model (Hong et al., 2009; Ershadi et al., 2013).

The "flux aggregation" approach was selected in this study. The fine resolution 8-day $ET_{RS,FAO56-PM}$ composites (30 m) were spatially aggregated to MODIS resolution (1 km) by applying three different aggregation methods: a) aggregation with mean function, b) aggregation with median function and c) nearest-neighbour resampling. The aggregated ET products were compared and evaluated against the original fine resolution images in order to identify which method gives the most "representative" coarse resolution images that would be used for the validation of the MOD16 product afterwards.

In the first method the mean value over an n-by-n moving window from the original raster image is the value of the coarse n-by-n pixel. In the second method the median value over an n-by-n moving window from the original raster image is the value of the coarse n-by-n pixel. Finally, in the nearest-neighbour resampling method the value of the coarse n-by-n pixel is the value that lies closest to the centroid of the n-by-n moving window (Bian and Butler, 1999).

The spatial aggregation was performed using the package "raster" on the R programming language (http://www.r-project.org/).

3.4.4 Comparison of input data to ET products

In an attempt to examine possible sources of error in the validation of the MOD16 ET product, a comparison is performed between the main input data used for the production of the two ET products examined in this thesis: a) $ET_{RS,FAO56-PM}$ and b) $ET_{RS,MOD16}$.

Both algorithms, FAO56-PM and MOD16, are based on the Penman-Monteith equation with the same canopy biophysical remote sensing inputs (LAI, albedo) and meteorological input data (net radiation,temperature, relative humidity), but from different sources and with different spatial scales. The comparison between the input data will further help the interpretation of the validation results and will provide insight into the quantitative differences between the two products.

Canopy and biophysical parameters

The MOD16 algorithm uses as inputs the LAI from MOD15A2 and the albedo from MCD43B3 (White-Sky-Albedo, NIR-band), both of which are average 8-day composites at 1 km spatial resolution. The FAO56-PM method has as inputs the LAI (hereafter called LAI-FAO56) and albedo (hereafter called albedo-FAO56) maps derived from Lansdat-8 images, as explained in Section 3.3. These two canopy biophysical parameters are considered constant for a time period of approximately seven days from the date of the satellite overpass (Vuolo et al., 2015).

The LAI and albedo maps derived from the available Landsat-8 images at DOY 140, DOY 188 and DOY 220 were selected for comparison, since they corresponded to the study period (DOY 145 to DOY 240). To perform a comparison between the LAI and albedo products used in the two algorithms, the products should be time matched and have the same spatial resolution. As a result, the LAI-FAO56 and albedo-FAO56 products derived from Landsat-8 were spatially aggregated to 1 km resolution (median value aggregation). Concerning the time period match, the selected MODIS products for comparison where those that corresponded to a similar time period with the Landsat products, specifically the MODIS products for DOY 137, DOY 185 and DOY 217. Finally, pixels with different land cover type than cropland were masked out using the MODIS Land Cover (MCD12Q1) product.

Meteorological inputs

The MOD16 algorithm uses as input the following MERRA-GMAO global daily meteorological data: a) daily temperature, b) relative humidity and c) net radiation. In order to evaluate the quality of these three MERRA-GMAO meteorological variables, hourly time series were extracted from the pixel of the EC station location (same pixel with the Groß-Enzersdorf weather station) for the time period from 25/5/2014 (DOY 145) to 28/8/2014 (DOY 240).

3.4.5 Validation of 8-day MOD16 ET product

The regional scale validation of MOD16 ET product is performed by comparing the twelve 8-day $ET_{RS,MOD16}$ composites, which cover the time period from 25/5/2014 (DOY 145) to 28/8/2014 (DOY 240), against the assumed to be "ground-truth" twelve 8-day $ET_{RS,FAO56-PM}$ composites for the same time period. The comparison is performed on a pixel-by-pixel basis in order to assess the accuracy of the MOD16 ET in both spatial extent and temporal evolution.

Furthermore, in order to investigate the impact of LAI and water availability on the estimated ET by the MOD16 product, a further evaluation of the 8-day $ET_{RS,MOD16}$ product was performed at a point-scale against the available ancillary ground-based measurements. The 8-day $ET_{RS,MOD16}$ and $ET_{RS,FAO56-PM}$ time series were extracted from the pixel where the ground-based measurements were conducted and also the EC station is located. From the same 1x1 pixel window a time series from the MOD15A2 LAI product was also extracted. Among

the available ancillary data were hourly rainfall (P) and volumetric soil water content (SWC) measurements. The SWC measurements examined in this case are those from the topsoil layer (0-10 cm), assuming that the evaporated soil moisture is mainly driven from precipitation. The hourly time series of rainfall (mm/hr) and SWC (%) from the topsoil layer (0-10 cm) were extracted from the same pixel as previous and two composites were created: a) 8-day sum of rainfall (mm/8day) and b) 8-day averaged SWC (%).

3.5 Statistical analysis

As part of the analysis undertaken in this thesis, a number of comparisons were performed between datasets. The comparisons were either between observed and estimated values, or between two datasets with estimated values. The comparisons included scatter plots and simple linear regression between two datasets. Visual interpretation of the scatter plots and the coefficients of linear regression (slope and intercept) were used to evaluate the linear relationship between the two datasets.

Furthermore, to assess the strength of the relationship between two datasets the following four statistical metrics were used:

1)Coefficient of determination (R^2)

$$R^2 = 1 - \frac{(\sum_{i=1}^{n}(Y_{o_i} - \overline{Y_o})(Y_{s_i} - \overline{Y_s}))^2}{\sum_{i=1}^{n}(Y_{o_i} - \overline{Y_o})^2 \sum_{i=1}^{n}(Y_{s_i} - \overline{Y_s})^2} \tag{3.5}$$

2)Root mean square error (RMSE)

$$RMSE = \sqrt{\frac{\sum_{i=1}^{n}(Y_{o_i} - Y_{s_i})^2}{n}} \tag{3.6}$$

3)Mean bias error (MBE)

$$MBE = \frac{\sum_{i=1}^{n}(Y_{s_i} - Y_{o_i})}{n} \tag{3.7}$$

4)Percent bias (PBIAS)

$$PBIAS = \frac{MBE}{\sum Y_{o_i}/n} \times 100 \tag{3.8}$$

where n represents the number of data values considered, Y_{s_i}, and Y_{o_i} represent the ith estimated and observed values, respectively, and $\overline{Y_o}$, $\overline{Y_s}$ represent average values of the corresponding variable.

The coefficient of determination (R^2) was computed to measure the strength of the relationship between the values of two datasets. The root mean square error (RMSE) and the mean bias error (MBE) quantify the difference between the values of two datasets. Especially, in the case of observed and estimated values they measure the deviation of estimated values from the observed. Finally, the percent bias (PBIAS) is the percentage of bias the values of one dataset show relative to the mean value of the other dataset.

The statistical analyses were performed on the R programming language (http://www.r-project.org/).

4 Results and discussion

The first section of this chapter presents the results of all the steps involved for the creation of the validated 8-day $ET_{RS,FAO56-PM}$ product at 1 km spatial resolution, which was used as reference for the validation of the 8-day $ET_{RS,MOD16}$. The second section provides the results of the comparison between the remotely sensed canopy biophysical parameters and the meteorological data used as inputs in the two RS-ET products examined in this thesis ($ET_{RS,FAO56-PM}$ and $ET_{RS,MOD16}$). Finally the last two sections are devoted to the MOD16 validation results at regional and point scale.

4.1 Implementation of FAO56-PM "one-step" approach

The four "analytical" Kc raster maps, as derived from the application of Equation 2.3, are shown in Figure 4.1. The maps have spatial resolution of 30 m and represent the state of the crops at pixel level for four different stages of the crop development during the year 2014.

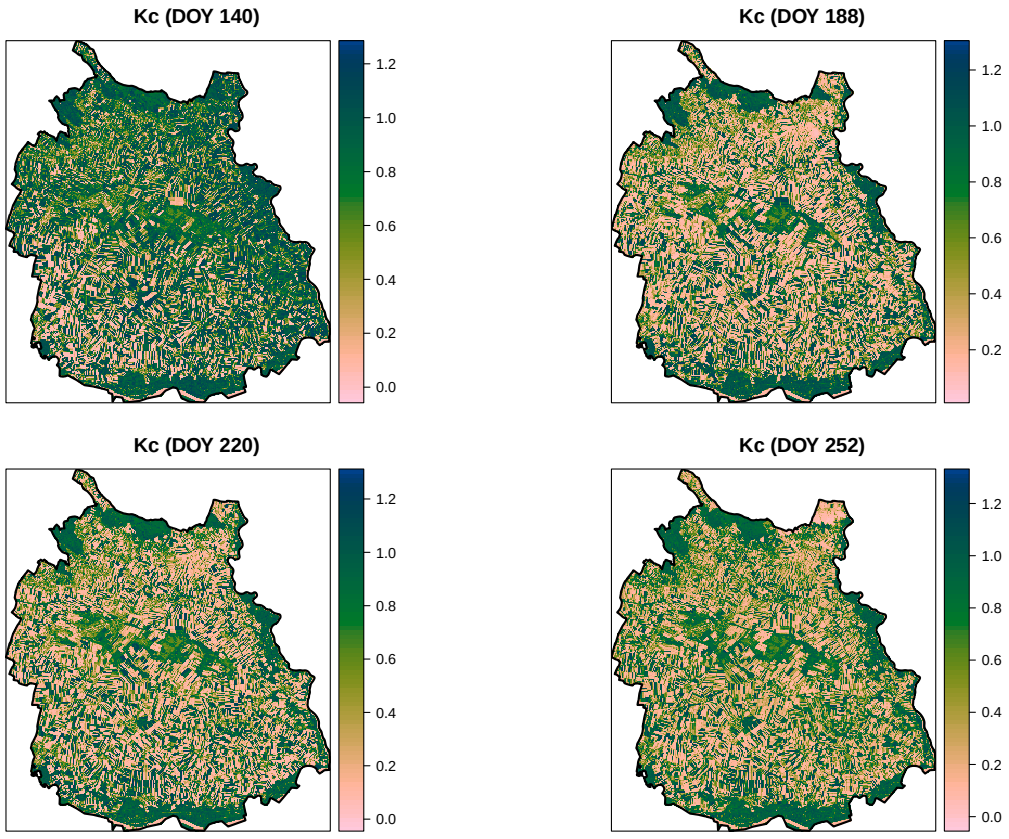

Figure 4.1: "Analytical" crop coefficient (Kc) raster maps representing four stages of the crop development during 2014. The four Kc maps were derived as the ratio of ET_c/ET_o, which were both calculated with the FAO56-PM equation for actual crop conditions and reference crop conditions, respectively. The biophysical crop parameters of the the actual crop conditions were derived from Landsat-8 images, from which the Kc maps also inherit their spatial resolution.

After the application of a pixel-wise linear interpolation between the above four Kc raster maps, 113 daily Kc raster maps were obtained. In order to visually inspect the resulting crop coefficient (Kc) curve from the linear interpolation, Kc values were extracted in form of time-series from the pixel where the EC station is located: a) for the four "analytical" Kc raster maps and b) for the interpolated Kc raster time series (Figure 4.2).

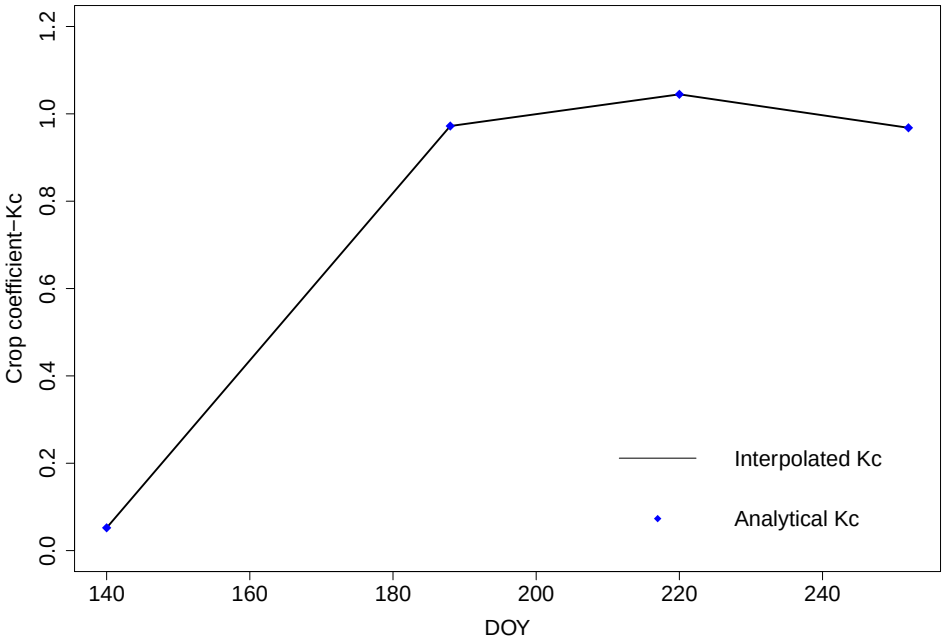

Figure 4.2: Crop coefficient (Kc) curve at the EC pixel location (maize field) calculated by linear interpolation between the four "analytical" Kc values. The continuous black line is the time-series extracted from the 113 Kc raster maps, while the blue squares is the time-series extracted from the four "analytical" Kc raster maps at DOY 140, DOY 188, DOY 220 and DOY 252.

The EC station used in this study was located in a maize field, thus the crop coefficient curve depicted in Figure 4.2 represents the Kc values of maize during the growing season of 2014. It can be seen that from DOY 140 to DOY 190 the Kc value is linearly increasing from a value close to 0 to a value of 1 with a steep slope, representing the crop development period where the crop grows. Afterwards, in the period from DOY 190 to DOY 220 the Kc value has a very slight increase, defining the mid-season stage. Finally, after DOY 220 the Kc value starts to descent, as the late season of the crop is under development.

The interpolated crop coefficient curve for maize follows the theoretical crop coefficient curve (Figure 3.6), while the values obtained at each crop development stage are in good agreement with the FAO-56 tabulated Kc values for maize, which are 1.15-1.20 for mid-season and around 1 for the end of the growing season (Allen et al., 1998).

In Figure 4.3 the aggregated daily ET_o, calculated with meteorological data from the Groß-Enzersdorf weather station, and the measured daily rainfall from the same weather station are plotted.

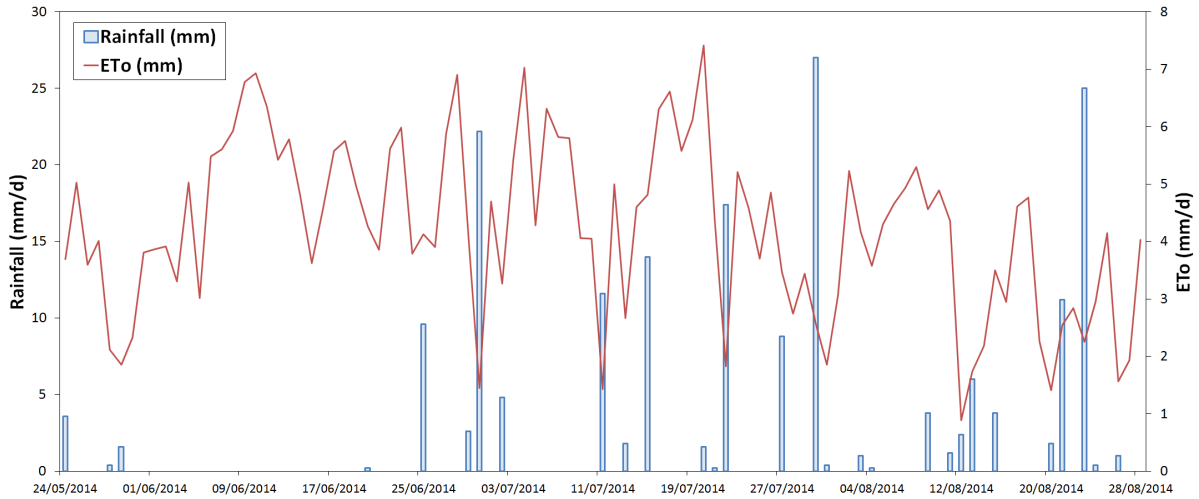

Figure 4.3: Time evolution of daily rainfall and reference evapotranspiration (ET_o) for the time period from 24/5/2014 (DOY 144) to 28/8/2014 (DOY 240) based on meteorological data from the weather station Groß-Enzersdorf (BOKU).

The total amount of ET_o during the time period from 24/5/2014 (DOY 144) to 28/8/2014 (DOY 240) is 408.5 mm, with a daily average value of 4.2 mm/d. The highest value observed is 7.41 mm/d at 20/7/2014 (DOY 201) and the lowest is 0.89 mm/d at 12/8/2014 (DOY 224). The total rainfall during the same period is 185.6 mm. High ET_o values are observed from May to middle July, as this period was warm and relatively dry. After the middle of July and until the end of August the climatic conditions (lower solar radiation and temperature) combined with the high amount of rainfall lead to lower ET_o values.

4.1.1 Point scale validation against EC measurements of ET

The validation of the hourly crop evapotranspiration maps (ET_c) was performed against eddy covariance measurements (EC) measurements of ET. In particular, Figure 4.4 presents the hourly time series of $ET_{RS,FAO56-PM}$ (mm/hr) and ET_{EC} (mm/hr) plotted against the hourly measured rainfall (mm/hr). Figure 4.5 shows the scatter plot of $ET_{RS,FAO56-PM}$ against ET_{EC}. In the two plots shown the hourly time series of $ET_{RS,FAO56-PM}$ was extracted on 1x1 pixel window. The statistical summary of the comparisons, including the results for both 1x1 and 3x3 pixel window, are given in Table 4.1.

As mentioned in the previous chapter, a quality flag was applied to the available latent heat (LE) flux measurements of the EC station reducing the number of valid ET_{EC} observations. Furthermore, in the comparisons between the $ET_{RS,FAO56-PM}$ and ET_{EC} time series only positive ET values were considered. In many cases negative values of hourly ET were observed and estimated at night times, denoting that the process of condensation was taking place. For the above reasons, the ET_{EC} time series, mostly, and the $ET_{RS,FAO56-PM}$ time series, in some parts, are not continuous.

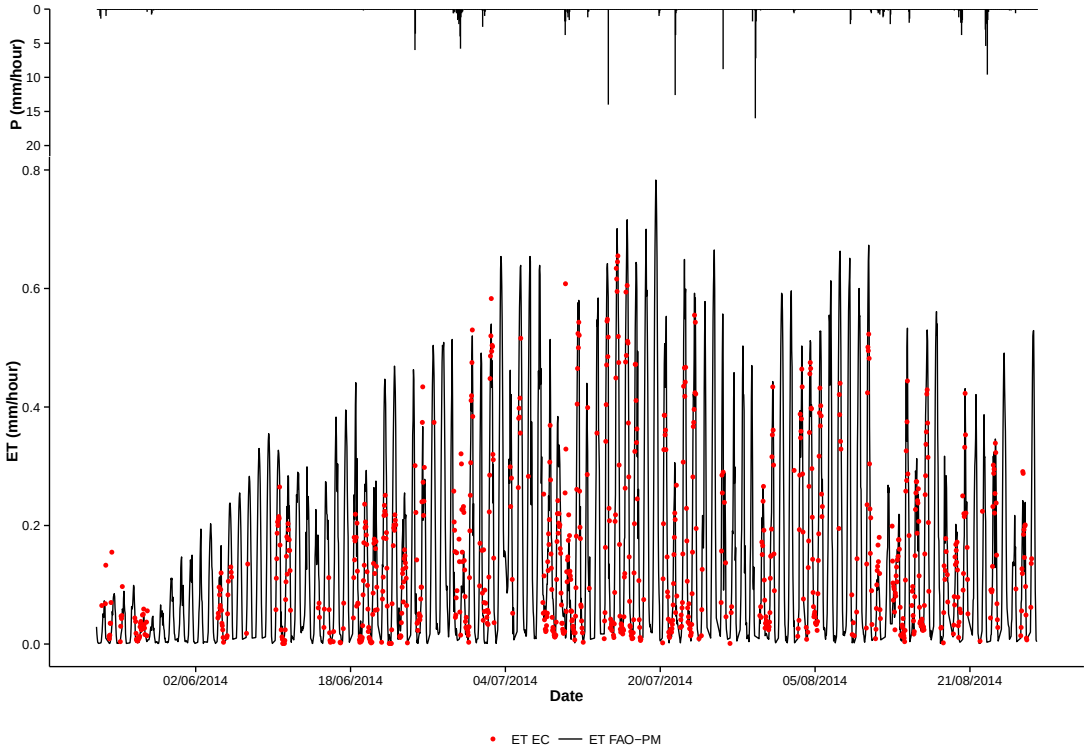

Figure 4.4: Comparison of valid hourly evapotranspiration measured by the EC station (red dots) and estimated crop evapotranspiration ET_c by using the FAO56-PM "one-step approach" extracted from the 1x1 pixel window of the EC station" (continuous black line).

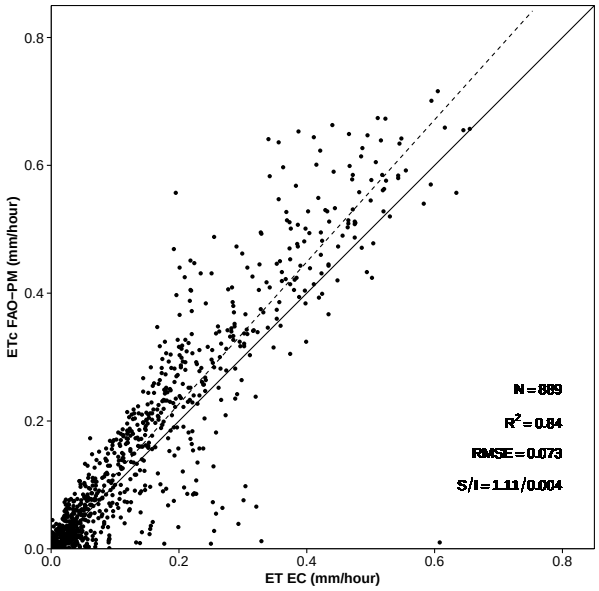

Figure 4.5: Scatter plot of the valid hourly evapotranspiration measured by the EC station and estimated crop evapotranspiration (ET_c) by using the FAO56-PM "one-step approach" extracted from the 1x1 pixel window of the EC station. The solid black line is the 1:1 line. The dashed black line shows the linear regression of the data points. The equation of the regression line, the R^2 and the RMSE between observed and estimated ET are given in the lower right corner of the figure.

Table 4.1: Statistical metrics of the comparison of ET_{EC} and $ET_{RS,FAO56-PM}$ at hourly time-step.

Pixel window	N (-)	R^2 (-)	RMSE (mm/hr)	MBE (mm/hr)	PBIAS (%)
1x1	889	0.84	0.07	0.02	14.04
3x3	889	0.84	0.07	0.02	13.92

The statistical metrics in Table 4.1 show that the extracted time series values of $ET_{RS,FAO56-PM}$, from both 1x1 and 3x3 pixel windows, gave almost the same results against the valid ET_{EC} measurements.

The comparison of $ET_{RS,FAO56-PM}$ estimations against valid ET_{EC} observations (Figure 4.5) indicate a good agreement with R^2 of 0.84, RMSE of 0.07 mm/hr and low values of MBE (0.02 mm/hr) and PBIAS (14%). The slope of the linear regression (>1) shows that the FAO56-PM 'one-step approach" method tends to overestimate higher ET values.

The FAO56-PM 'one-step approach" satisfactory reproduced the temporal evolution of measured ET values during most of the study period (Figure 4.4). Better performance was achieved at drought periods when low ET values are observed and ET is mainly due to transpiration. Higher discrepancies can be seen after rainfall events, when high ET values are observed due to soil evaporation processes which cannot be reproduced by models based on the FAO56-PM approach. An example is given in the following table (Table 4.2) showing the great differences in observed ET from the EC station and modelled from the FAO56-PM "one-step approach" method, during a day with heavy rainfall. It can be seen that high rainfall, with prevailing meteorological conditions result in high hourly ET, with values exceeding 0.2 mm/hr. On the other hand it is clearly observed that the modelled ET values don't absorb the soil evaporation dynamics during these 13 hours, having an average bias of -0.085 mm/hr and reaching a bias of -0.25 mm/hr on 30/6 11:00 hour.

Table 4.2: Measured climatic variables and ET, estimated ET and parameters of FAO56-PM for the 30th of June 2014 from 07:00 to 19:00.

	Measured					FAO-56 PM		
Date Time	Rn (mm/hr)	P (W/m^2)	RH (%)	Temp (C)	ET (mm/hr)	ET_o (-)	Kc (mm/hr)	ET_c (mm/hr)
30/6 07:00	11.8	1.8	99.3	12.9	0.05	0.02	0.84	0.02
30/6 08:00	10.8	4	99.9	12.8	0.03	0.02	0.84	0.02
30/6 09:00	34.1	5.8	99.9	13	0.02	0.03	0.84	0.03
30/6 10:00	146.7	1.2	99.9	13.5	0.32	0.08	0.84	0.07
30/6 11:00	227.9	0.2	99.9	14.5	0.3	0.12	0.84	0.1
30/6 12:00	194.9	0.6	99.9	14.8	0.23	0.1	0.84	0.09
30/6 13:00	175	0	96.6	15.8	0.16	0.12	0.84	0.1
30/6 14:00	127.4	0.4	88.1	16	0.14	0.1	0.84	0.09
30/6 15:00	211.6	0.2	91.9	16.3	0.23	0.13	0.84	0.11
30/6 16:00	269.3	0	81.8	17.7	0.23	0.19	0.84	0.16
30/6 17:00	242.5	0	75.3	18.3	0.22	0.18	0.84	0.15
30/6 18:00	108.6	0	76.6	17.8	0.14	0.11	0.84	0.09
30/6 19:00	44.1	0	72.9	17.5	0.13	0.09	0.84	0.07

4.1.2 Spatial and temporal aggregation of $ET_{RS,FAO56-PM}$

After the temporal aggregation performed in the hourly $ET_{RS,FAO56-PM}$ product, twelve 8-day $ET_{RS,FAO56-PM}$ composites were created (Table 4.3) for the time period from 25/5/2014 (DOY 145) to 28/8/2014 (DOY 240).

Table 4.3: The 8-day $ET_{RS,FAO56-PM}$ composites created for the validation of 8-day $ET_{RS,MOD16}$ composites.

1) DOY 145 $ET_{RS,FAO56-PM}$	7) DOY 193 $ET_{RS,FAO56-PM}$
2) DOY 153 $ET_{RS,FAO56-PM}$	8) DOY 201 $ET_{RS,FAO56-PM}$
3) DOY 161 $ET_{RS,FAO56-PM}$	9) DOY 209 $ET_{RS,FAO56-PM}$
4) DOY 169 $ET_{RS,FAO56-PM}$	10) DOY 217 $ET_{RS,FAO56-PM}$
5) DOY 177 $ET_{RS,FAO56-PM}$	11) DOY 225 $ET_{RS,FAO56-PM}$
6) DOY 185 $ET_{RS,FAO56-PM}$	12) DOY 233 $ET_{RS,FAO56-PM}$

These twelve 8-day $ET_{RS,FAO56-PM}$ composites were spatially aggregated from the 30 m resolution to the 1 km resolution of the MOD16 produts. The evaluation of the three spatial aggregation methods and the influence each method has on the final coarse resolution evapotranspiration product was assessed with density plots, statistical measures and visual inspection of the aggregated rasters. The statistical measures used in this analysis included the mean, standard deviation (Std), minimum (min) and maximum (max) values of each raster.

Density plots

With the use of density plots the distribution of ET values from the native resolution raster data and the aggregated products can be visualized and the changes in the variance within each raster dataset can be investigated.

For each of the twelve DOYs, representing an 8-day period, the following density plots were constructed and overlaid: i) the native resolution product with 30 m resolution, ii) the aggregated product with mean value at 1 km resolution, iii) the aggregated product with median value at 1 km resolution and iv) the resampled product with Nearest-Neighbour (NN) at 1 km. Below each figure the statistical measures of each product are provided for a quantitative examination.

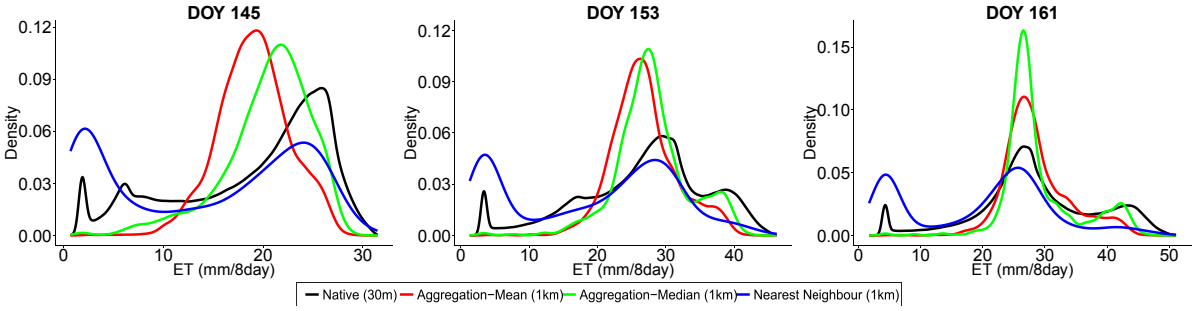

	DOY 145				DOY 153				DOY 161			
	NAT (30m)	AGGR-MN (1km)	AGGR-MD (1km)	NN (1km)	NAT (30m)	AGGR-MN (1km)	AGGR-MD (1km)	NN (1km)	NAT (30m)	AGGR-MN (1km)	AGGR-MD (1km)	NN (1km)
Mean	19.03	19.04	20.46	14.22	26.81	26.83	28.01	19.37	28.55	28.56	29.00	19.67
Std	7.59	3.53	4.36	9.71	9.23	4.77	5.34	11.97	9.65	5.27	5.97	11.50
Min	0.69	2.57	1.79	1.55	1.31	4.29	3.24	2.90	1.70	5.19	4.13	3.26
Max	31.46	28.55	28.82	31.33	46.22	41.87	42.25	45.80	51.08	46.15	46.56	50.35

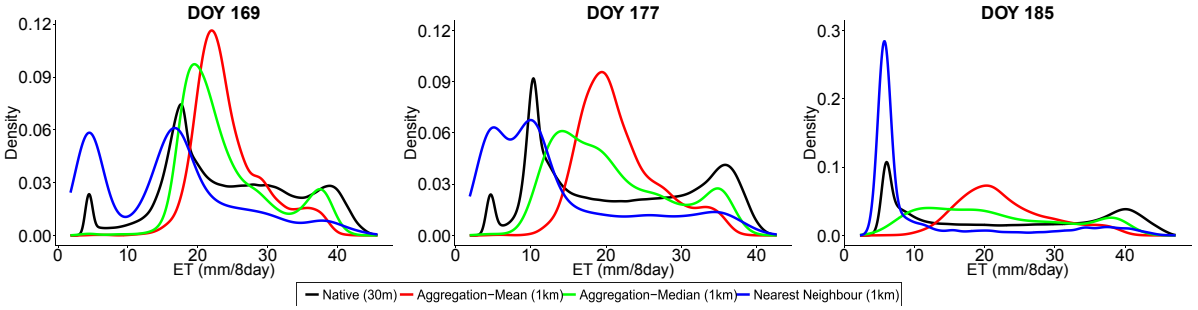

	DOY 169				DOY 177				DOY 185			
	NAT (30m)	AGGR-MN (1km)	AGGR-MD (1km)	NN (1km)	NAT (30m)	AGGR-MN (1km)	AGGR-MD (1km)	NN (1km)	NAT (30m)	AGGR-MN (1km)	AGGR-MD (1km)	NN (1km)
Mean	24.43	24.44	24.02	15.95	21.79	21.78	20.91	13.61	22.83	22.82	21.55	11.68
Std	9.45	5.07	6.57	9.81	10.59	5.34	7.73	9.82	13.65	6.54	9.97	10.93
Min	1.78	5.10	4.24	2.76	1.90	5.16	4.45	3.21	2.24	5.96	5.25	4.26
Max	45.71	41.13	41.52	44.25	42.67	38.22	38.57	40.54	47.20	41.49	41.92	46.01

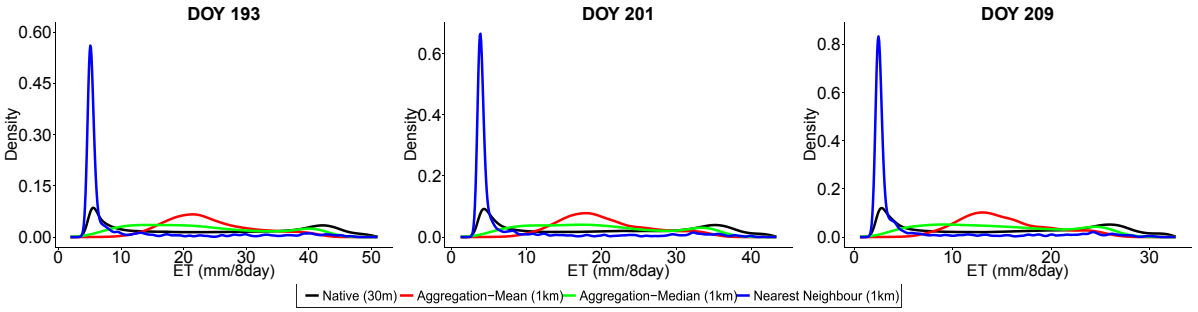

	DOY 193				DOY 201				DOY 209			
	NAT (30m)	AGGR-MN (1km)	AGGR-MD (1km)	NN (1km)	NAT (30m)	AGGR-MN (1km)	AGGR-MD (1km)	NN (1km)	NAT (30m)	AGGR-MN (1km)	AGGR-MD (1km)	NN (1km)
Mean	24.21	24.19	23.03	10.16	20.42	20.39	19.60	8.17	15.20	15.18	14.63	5.86
Std	14.70	7.05	10.57	10.56	12.46	5.96	8.85	9.03	9.52	4.50	6.77	6.94
Min	1.93	5.96	5.11	3.99	1.25	4.68	3.88	3.16	0.59	3.17	2.51	1.97
Max	50.98	43.80	44.42	47.32	43.34	36.60	38.38	41.54	32.66	27.65	29.65	30.63

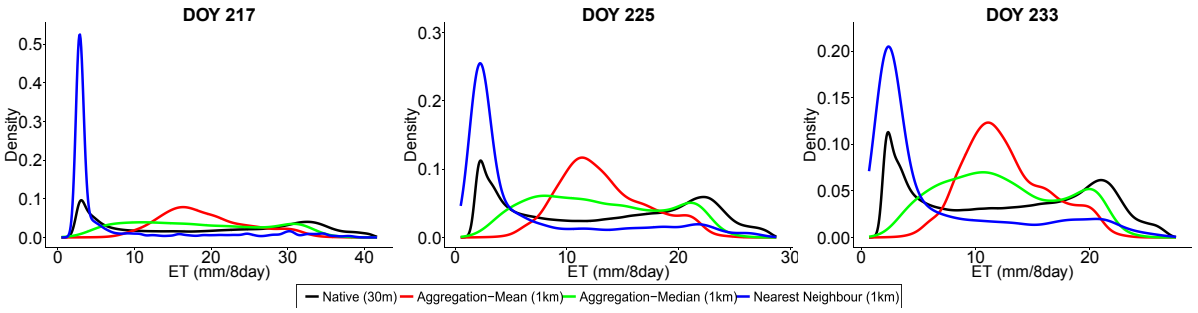

	DOY 217				DOY 225				DOY 233			
	NAT (30m)	AGGR-MN (1km)	AGGR-MD (1km)	NN (1km)	NAT (30m)	AGGR-MN (1km)	AGGR-MD (1km)	NN (1km)	NAT (30m)	AGGR-MN (1km)	AGGR-MD (1km)	NN (1km)
Mean	19.22	19.19	18.48	7.45	13.29	13.27	12.92	6.46	12.67	12.65	12.38	6.60
Std	12.33	5.76	8.78	9.16	8.10	3.91	5.75	6.87	7.44	3.70	5.23	6.51
Min	0.46	3.74	2.80	1.94	0.49	2.74	2.11	1.45	0.68	2.78	2.20	1.39
Max	41.65	36.32	38.37	38.97	28.75	24.88	25.32	27.88	27.53	23.51	23.99	27.07

Figure 4.6: Density plots and basic statistical measures of the native resolution (NAT) 8-day $ET_{RS,FAO56-PM}$ and the aggregated 8-day $ET_{RS,FAO56-PM}$ composites using the the mean value aggregation (AGGR-MN), the median value aggregation(AGGR-MD) and Nearest Neighbour (NN) resampling.

Based on the density plots and the statistics from Figure 4.6 useful conclusion can be drawn regarding the effects of each spatial aggregation method on the native resolution (30 m) ET raster map. The mean aggregation method "smooths" the original data and therefore produces a bell-shaped curve density plot, in all cases. The mean aggregation also reduces the variance of the values (spatial variance) having much smaller standard deviation, almost half (approximately 50% smaller), compared with the standard deviation of the native resolution raster. The median aggregation produces better results regarding the standard deviation, with values closer to the Standard deviation values of the native resolution raster. This has a direct impact to the min and max values of the aggregated product, which are also closer to the ones from the native resolution. Furthermore, from the observation of the first six DOYs it can be clearly denoted that the density plot of the aggregated raster with median follows the pattern of the native resolution density plot more accurate than the one obtained from the mean aggregation method. Finally, the nearest neighbour Std, min and max statistical metrics are the closest to those of the native resolution raster ET in all 12 DOYs. Also, the pattern of the density function resembles that of the native resolution raster in the initial cases, but after DOY 185 as the lower ET pixel values are the majority in the image the NN resampling method overestimates these low ET values and the produced aggregated image has very large errors. These results indicate that NN resampling is not a suitable method for aggregating continuous data, as evapotranspiration.

Raster maps

To further explore the effects of spatial aggregation from fine resolution (30 m) to coarse resolution (1 km), the raster ET maps of the native resolution and the aggregated 1 km resolution are shown for each method at 3 DOYs during the study period.

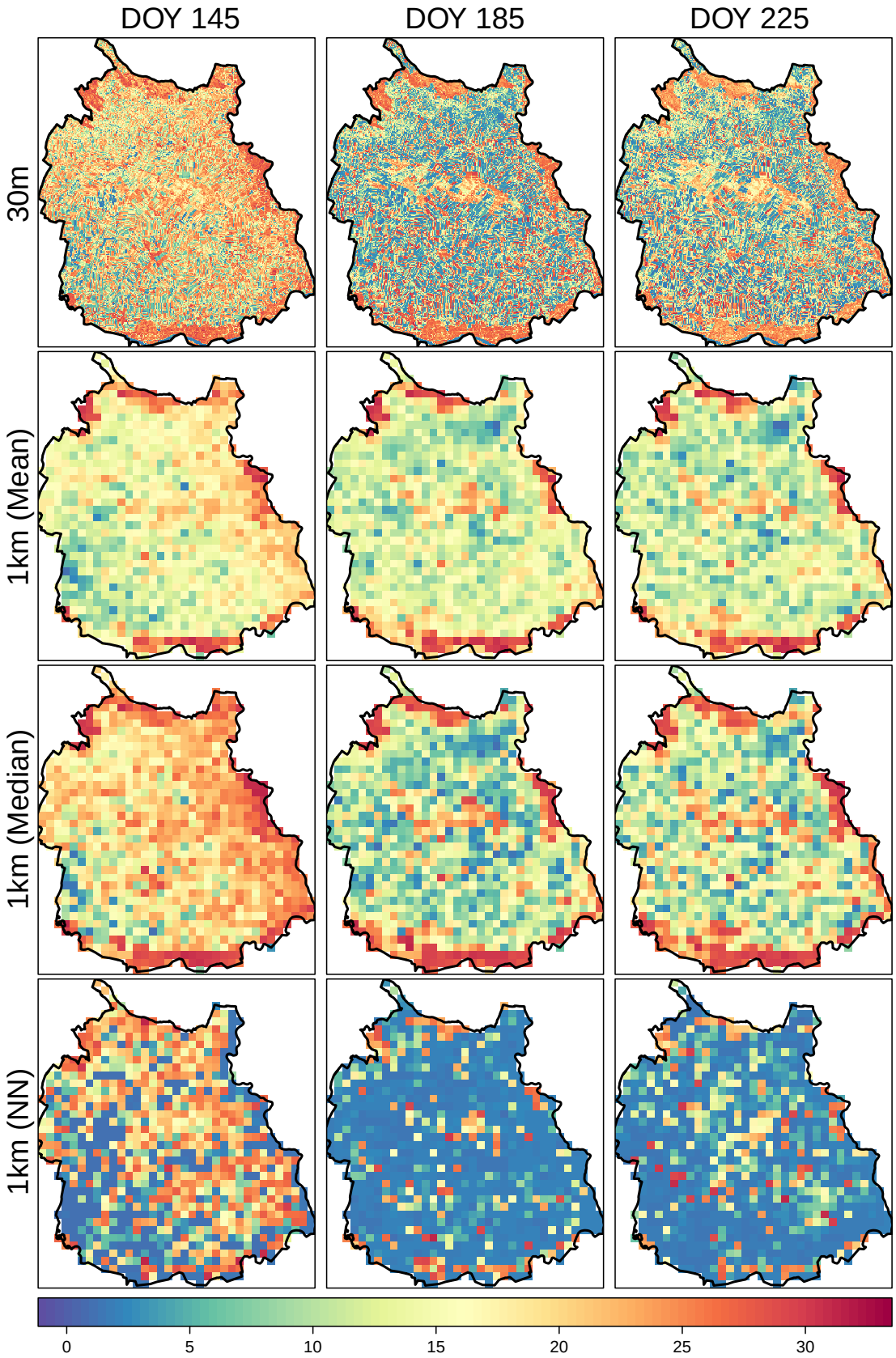

Figure 4.7: Raster maps of 8-day $ET_{RS,FAO56-PM}$ for the study area at DOY 145, DOY 185 and DOY 225 with native resolution (30 m) and coarse resolution (1 km) after aggregation with the mean value (Mean), median value (Median) and Nearest Neighbour (NN).

Observing Figure 4.7 it is clear that among the three methods the nearest neighbour resampling technique has the worst performance by far, producing aggregated maps which underestimate

ET and are almost homogeneous. Between the mean and median aggregation method, the latter one seems to represent better the spatial pattern of ET in the study area.

Based on all the above findings from the statistical analysis, the visual inspection of the density plots and the raster maps, the aggregation with median value performed better in respect of preserving the statistical characteristics of the native resolution ET maps. Therefore, the 8-day $ET_{RS,FAO56-PM}$ aggregated at 1 km resolution with the median value was selected for the validation of the 8-day $ET_{RS,MOD16}$ at regional scale.

4.2 Input comparison

4.2.1 Canopy biophysical parameters

Figure 4.8 illustrates the pixel-by-pixel comparison of MODIS LAI (MOD15A2) and LAI-FAO56 for three time periods and Figure 4.9 illustrates the pixel-by-pixel comparison of MODIS albedo (MCD43B3) and albedo-FAO56 for three time periods.

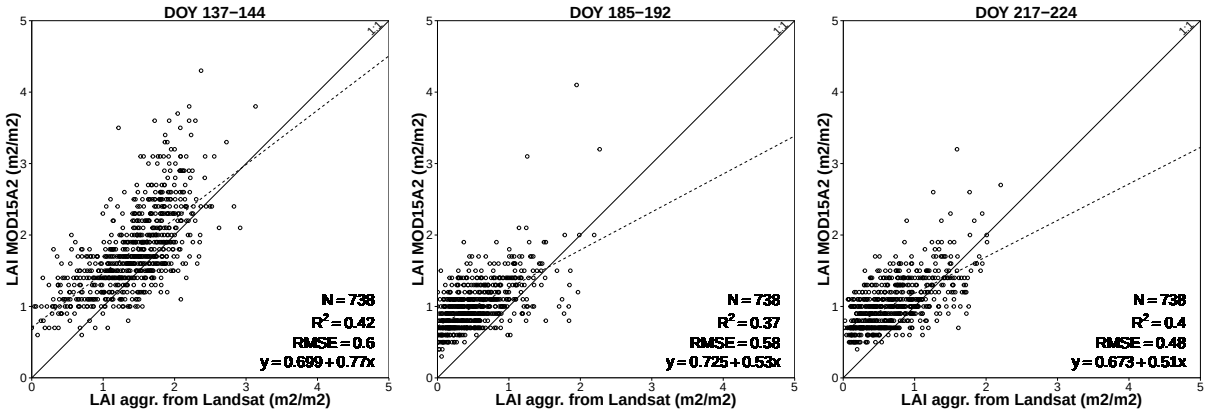

Figure 4.8: Comparison of LAI input to MOD16 and FAO56-PM algorithms. Scatter plot between the aggregated 1 km resolution LAI maps derived from Landsat-8 and the MOD15A2 LAI products at three time periods (DOY 137, DOY 185, DOY 217).

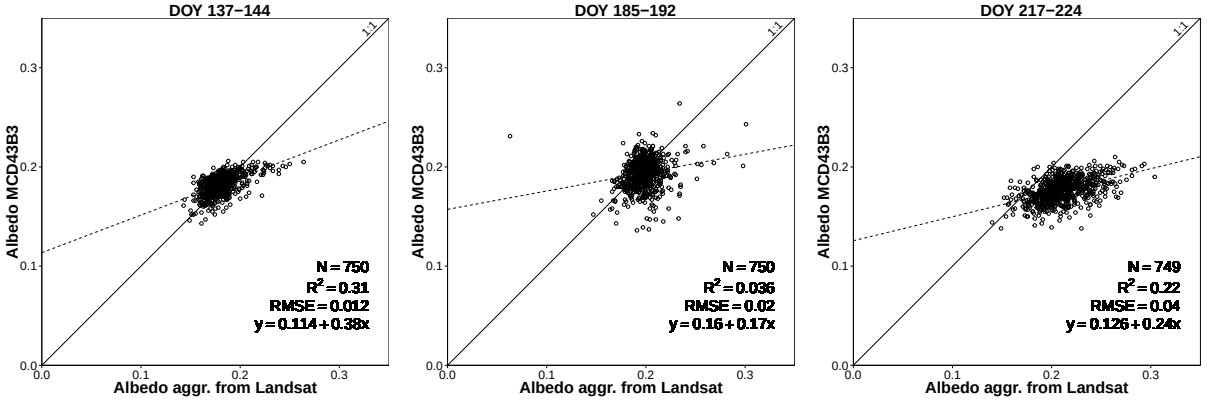

Figure 4.9: Comparison of albedo input to MOD16 and FAO56-PM algorithms. Scatter plot between the aggregated 1 km resolution albedo maps derived from Landsat-8 and the MCD43B3 albedo products at three time periods (DOY 137, DOY 185, DOY 217).

It should be notated that the comparisons between the LAI and albedo inputs to the two algorithms have a very high degree of uncertainty. This is due to the different methods/models

applied to derive the LAI and albedo products from the MODIS and Landsat data, which were not examined extensively since this was not the scope of the thesis. Also, the aggregation processes and the inaccurate time match further extend this uncertainty.

The results of the comparison between the LAI inputs, shown in Figure 4.8, indicate a poor agreement between the MODIS LAI and LAI-FAO56, with an average R^2 value of 0.4 and RMSE ranging from 0.5 to 0.6. The most interesting finding is that MODIS LAI is almost always systematically higher than the FAO56-LAI, in all three time period comparisons.

The results of the comparison between the albedo inputs, shown in Figure 4.9, indicate that there is no linear relation between the MODIS albedo and albedo-FAO56. This is explained by the very small range of values for both products, on the order of 0.05-0.08, and the homogeneity of values across the study area, as it is consists only of croplands.

4.2.2 Meteorological inputs

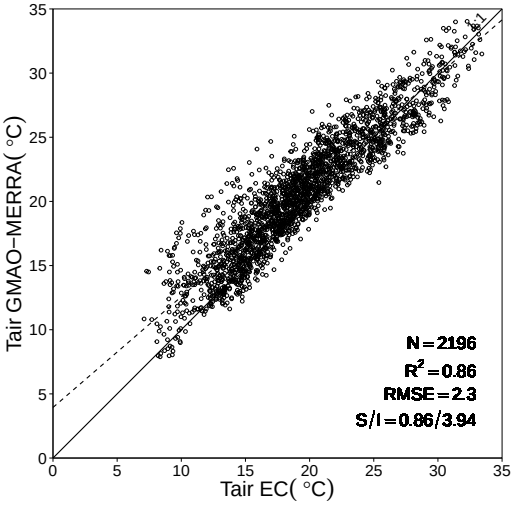

(a) Scatter plot of measured and MERRA-GMAO air temperature (T_{air}).

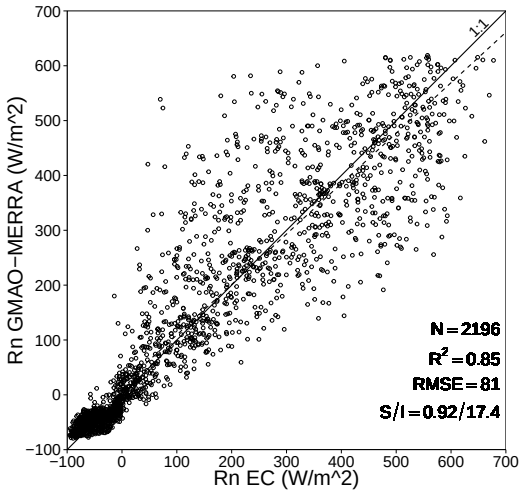

(b) Scatter plot of measured and MERRA-GMAO net radiation(R_n).

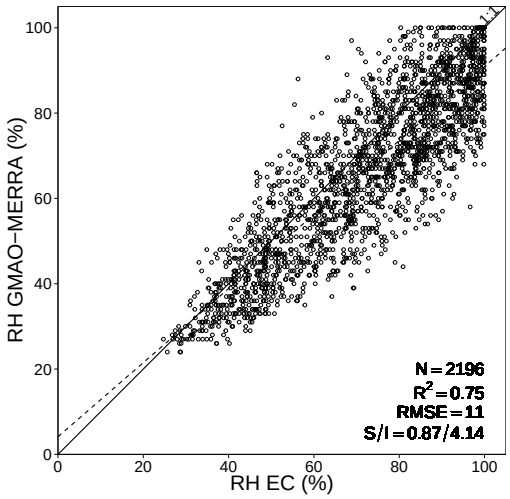

(c) Scatter plot of measured and MERRA-GMAO relative humidity(RH).

Figure 4.10: Comparison between the hourly measured meteorological variables and the hourly MERRA-GMAO meteorological variables extracted from the EC station pixel location for the time period between 25/5/2014 and 28/8/2014.

The hourly time-series of a) daily temperature (°C), b) relative humidity (%) and c) net radiation (W/m^2) were compared against ground-based hourly measurements of the same meteorological variables in the following scatter plots (Figure 4.10).

For all three meteorological variables a high degree of agreement is observed between measured and MERRA-GMAO time-series. The results for air temperature (T_{air}) indicated a high R^2 value of 0.86 and RMSE of 2.3°C. The very good agreement between measured and MERRA-GMAO air temperature is further confirmed by the spread of the points around the 1:1 line which is almost perfect. Only a small overestimation by the MERRA-GMAO data can be seen for air temperatures ranging from 6 to 20 °C. The results for net radiation (R_n) also indicated a high R^2 value of 0.86 but in this case the RMSE is also high with a value of 81 W/m^2. The scatter between the 1:1 line further confirms this, implying that there are great differences between some hourly measurements and the MERRA-GMAO values. Finally, the results of the relative humidity (RH) showed a relatively high R^2 value of 0.75, proving consistency between the two time-series, and relatively low RMSE of 11%. Based on the slope of the linear regression line the MERRA-GMAO underestimates high RH values (>70%).

4.3 Regional scale validation of 8-day MOD16 ET product

4.3.1 Spatio-temporal distributions of ET_{MOD16} and $ET_{FAO56\text{-}PM}$

In order to assess the spatial and temporal distribution of ET from $ET_{RS,FAO56-PM}$ and $ET_{RS,MOD16}$ products the regional 8-day ET raster maps are illustrated in Figure 4.11. Alongside the raster maps of each product, the difference in ET (mm/8day) between them is also mapped. The ET raster maps have spatial resolution of 1 km and pixels with different land cover type than cropland are masked out using the MODIS Land Cover (MCD12Q1) product.

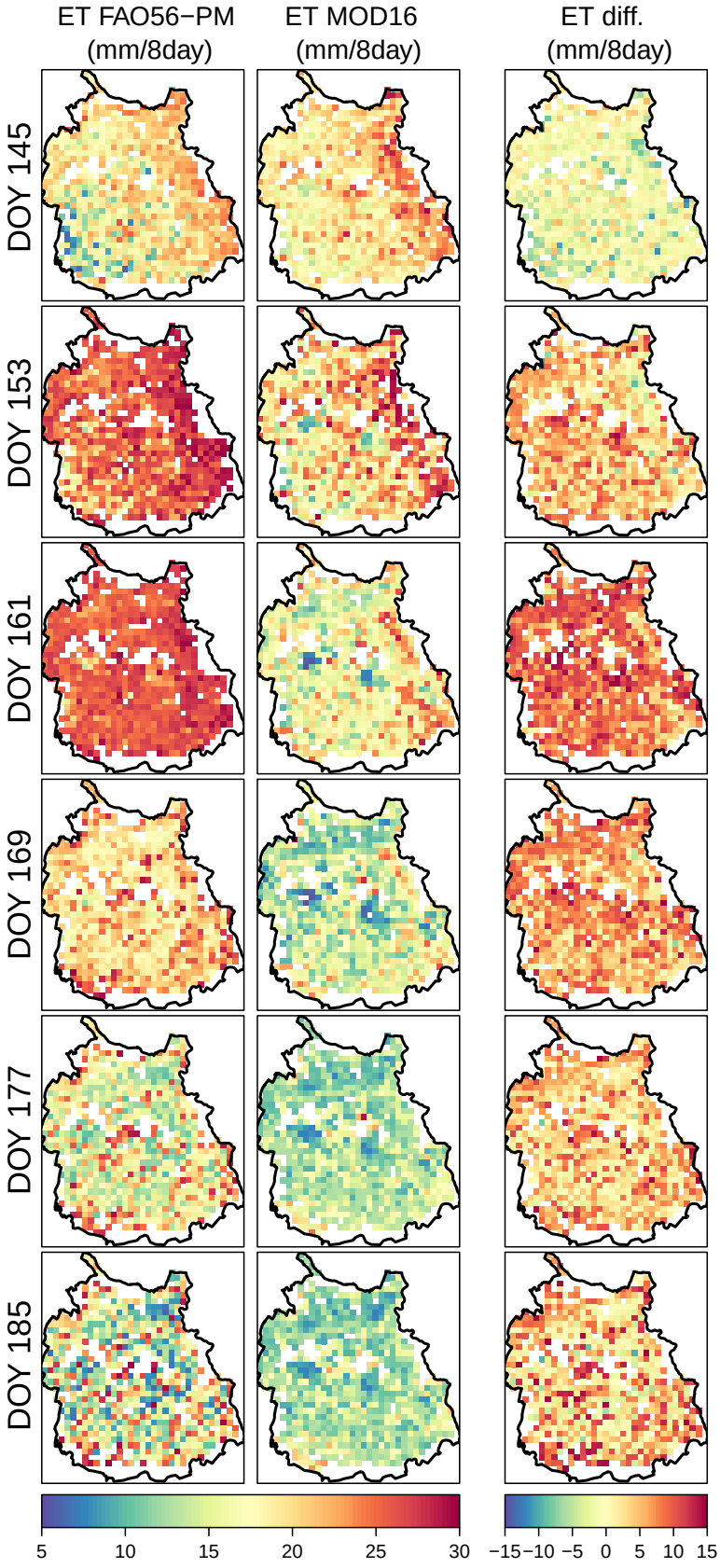

Figure 4.11: 8-day ET raster maps of $ET_{RS,FAO56-PM}$ (left), $ET_{RS,MOD16}$ (center) and their difference (right) over the Marchfeld region for the time period from 25/5/2104 (DOY 145) - 28/8/2014 (DOY 240). The maps have 1 km spatial resolution.

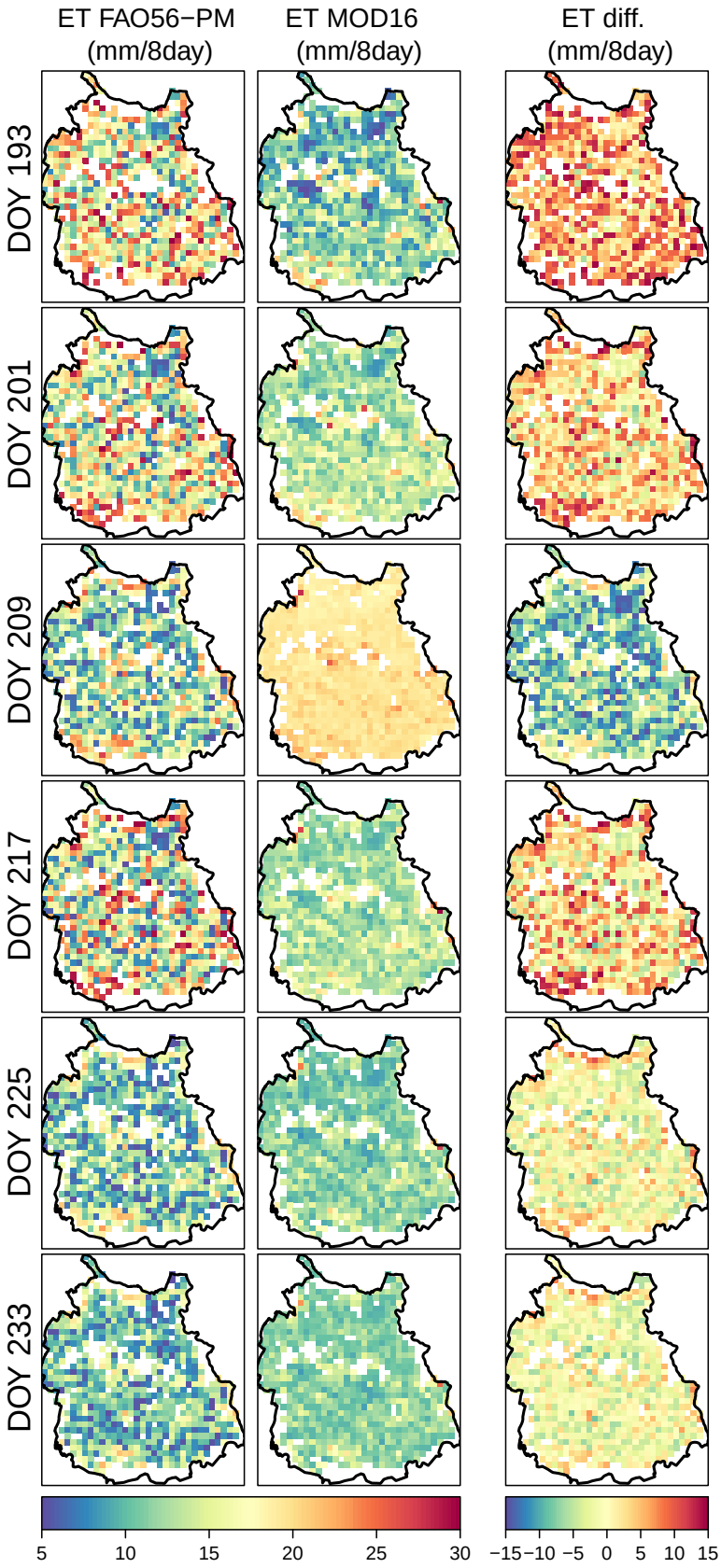

Figure 4.11: (continued).

In addition to Figure 4.11, boxplots (or Box-and-Whisker Plots) showing the distribution of ET for each 8-day composite of the two products were constructed. The solid line across the box represents the median value, and the box is delimited by the quartiles and the whiskers by the extreme values. The hollow circles represent outliers.

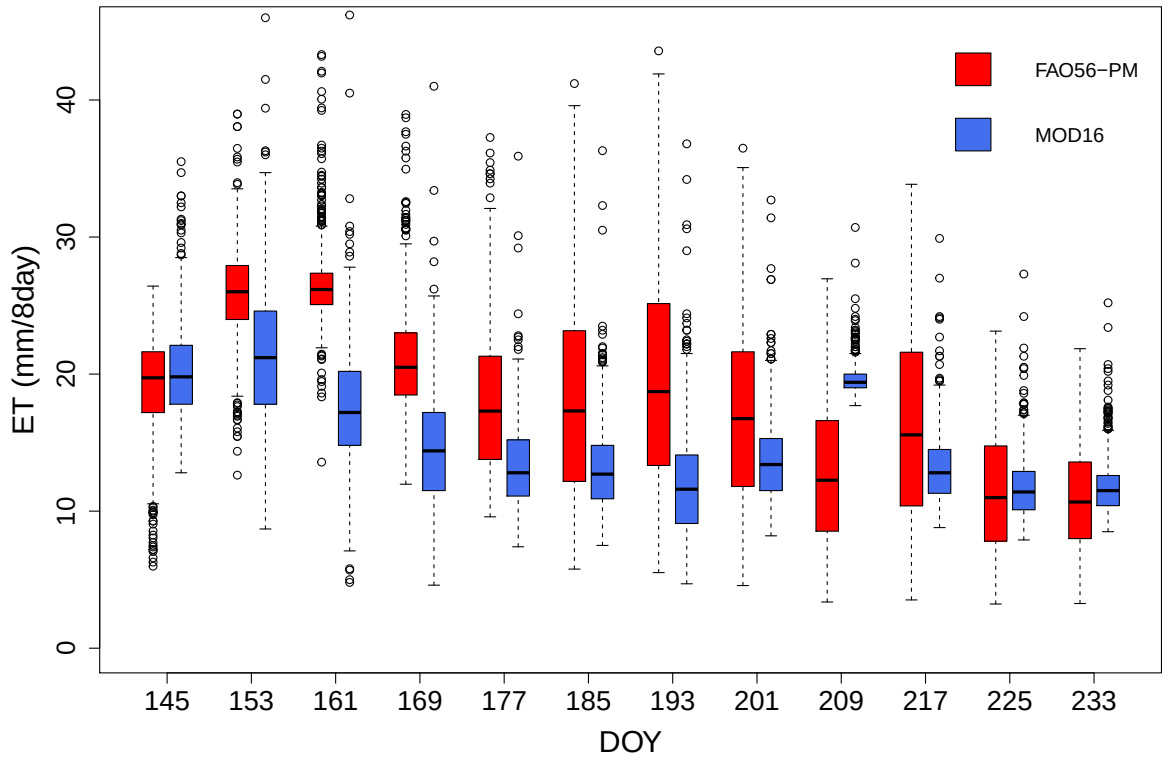

Figure 4.12: Boxplots showing the distribution of ET values (mm/8day) for each 8-day composite of $ET_{RS,FAO56-PM}$ (red) and $ET_{RS,MOD16}$ (blue) that was used in the validation process.

From the observation of the raster maps (Figure 4.11) and the boxplots (Figure 4.12) conclusions regarding the spatio-temporal distribution of ET between the two products can be made. Both products show similar temporal evolution of ET during the study period. Both products display high ET values during the first three 8-day periods, from DOY 145 to DOY 161, with average ET values ranging from 19.5 to 26 mm/8day for $ET_{RS,FAO56-PM}$ and from 17.2 to 21.2 mm/8day for $ET_{RS,MOD16}$, respectively. After the first three 8-day periods, the $ET_{RS,FAO56-PM}$ product shows a sharp decrease dropping from an average value of 26 mm/8day at DOY 161 to 20.5 mm/8day at DOY 169. In the following DOYs ET decreases steadily, reaching an average value of 10 mm/8day at the end of the study period (DOY 233). The $ET_{RS,MOD16}$ product shows similar behaviour, with the difference that ET decreases gradually after DOY 161 until the end of the study period at DOY 233. Its average value during this period is about 13 mm/8day. In Figure 4.12 it can be observed that there is one 8-day $ET_{RS,MOD16}$ product, at DOY 209, which doesn't follow the previously mentioned trend. At that 8-day period there is steep increase in average ET from 13.4 at DOY 201 to 19.4 mm/8day at DOY 209 and then a steep decrease to 13 mm/8day at DOY 217.

The fact that $ET_{RS,FAO56-PM}$ boxplots in most 8-day periods are much higher than the boxplots of $ET_{RS,MOD16}$, indicate the greater variability in range of values for the $ET_{RS,FAO56-PM}$ products compared to the ones from MOD16. The only exception are the boxplots of $ET_{RS,FAO56-PM}$ at DOYs 153 and 161, where the range of values is short and the estimated ET is very high across the entire Marchfeld region (Figure 4.11).

This variability of pixel values can be further seen in the raster maps (Figure 4.11), where on the one side the $ET_{RS,FAO56-PM}$ raster maps have a very "mixed" pattern of pixel values for the Marchfeld region and on the other side those from MOD16 have a very homogeneous pattern for the whole region. The main reason for this variability is that $ET_{RS,FAO56-PM}$ raster maps were created from the implementation of the FAO56-PM "one-step approach" to fine resolution imagery (Landsat-8), at a high temporal scale (daily time step), capturing the spatial and temporal variability of ET at a pixel/field scale.

Therefore, even after the temporal and spatial aggregation processes, this variability is visible in some extent in the 8-day $ET_{RS,FAO56-PM}$ raster maps with 1 km spatial resolution. On the other hand the MOD16 algorithm has coarse resolution (1 km) input data which cannot capture the dynamics of ET at pixel scale and this is evident in the resulted 8-day $ET_{RS,MOD16}$ raster maps.

4.3.2 Pixel-by-Pixel comparison

The regional scale validation of MOD16 ET product is performed by the pixel-by-pixel comparison of the twelve 8-day $ET_{RS,MOD16}$ composites, which cover the time period from 25/5/2014 (DOY 145) to 28/8/2014 (DOY 240), against the twelve 8-day $ET_{RS,FAO56-PM}$ composites for the same time period.

The scatter plots shown in Figure 4.13 are used for quantitative evaluation of the estimated ET from 8-day $ET_{RS,MOD16}$ against the assumed "ground-truth" 8-day $ET_{RS,FAO56-PM}$, in space and time. The statistical summary of the validation is also presented more comprehensively in Table 4.4.

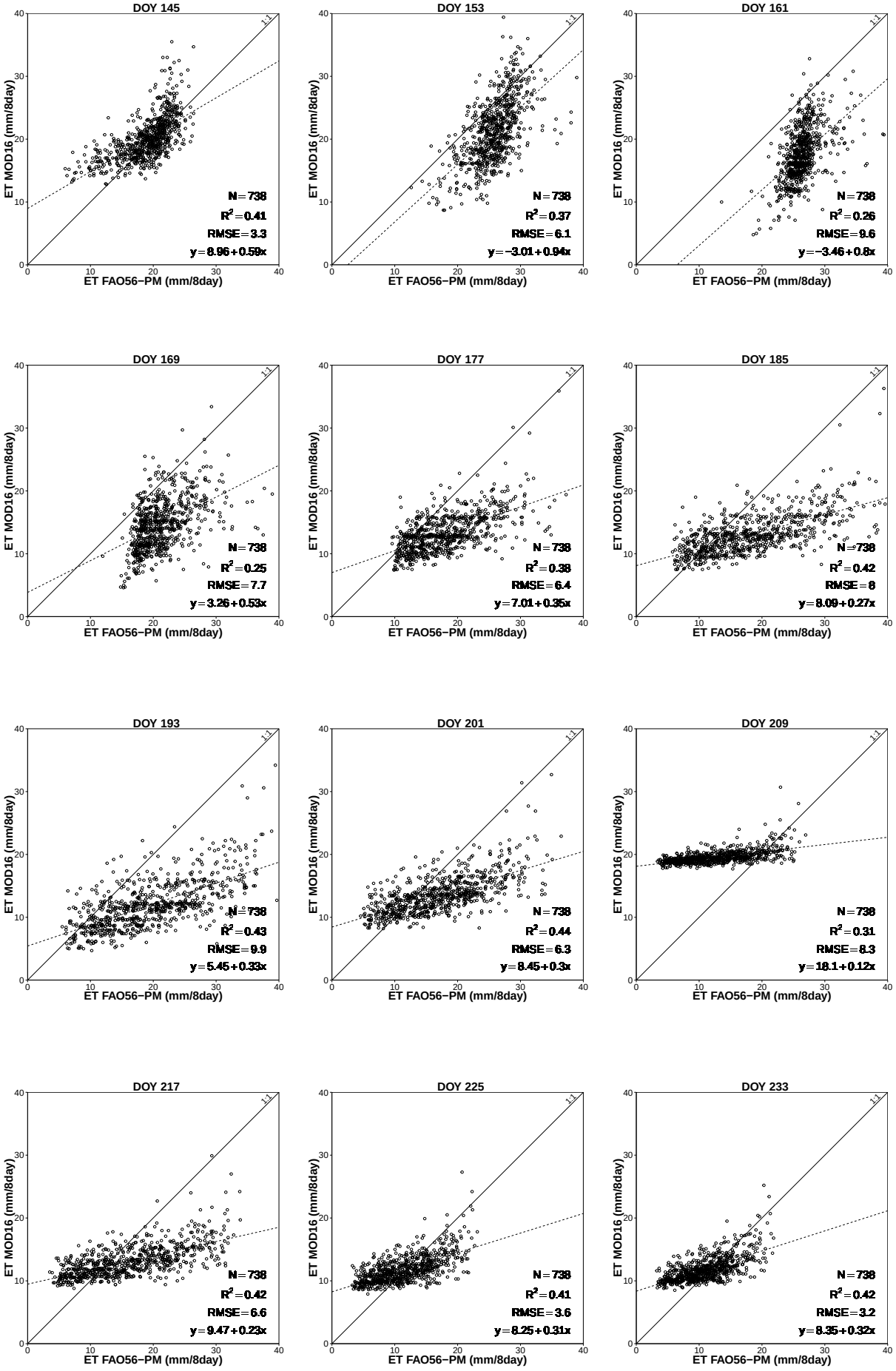

Figure 4.13: Scatter plots of 8-day $ET_{RS,MOD16}$ against the assumed "ground-truth" 8-day $ET_{RS,FAO56-PM}$ for 12 DOYs covering the period from 25/5/2104-28/8/2014.

Table 4.4: Validation results of 8-day $ET_{RS,MOD16}$ against the assumed "ground-truth" 8-day $ET_{RS,FAO56-PM}$ for 12 DOYs covering the period from 25/5/2104-28/8/2014.

DOY	No. of pixels	R^2 (-)	RMSE (mm/8day)	Mean bias error (mm/8day)	PBias (%)
145	738	0.41	3.26	1.11	5.85
153	738	0.37	6.08	-4.50	-17.39
161	738	0.26	9.64	-8.85	-33.41
169	738	0.25	7.74	-6.64	-31.23
177	738	0.38	6.39	-4.75	-26.30
185	738	0.42	7.97	-5.21	-28.53
193	738	0.43	9.88	-7.78	-39.26
201	738	0.44	6.27	-3.53	-20.61
209	738	0.31	8.28	6.75	52.54
217	738	0.42	6.62	-3.09	-19.05
225	738	0.41	3.58	0.38	3.34
233	738	0.42	3.23	0.91	8.32
Average	738	0.38	6.58	-2.93	-12.14

Looking at the scatter plots and taking the coefficient of determination (R^2) as a measure for the performance of $ET_{RS,MOD16}$ against the assumed "ground-truth" $ET_{RS,FAO56-PM}$ it can be concluded that the performance of MOD16 is relatively poor, with R^2 values lower than 0.5 in all twelve DOYs (8-day periods). The R^2 values varied from 0.25 (DOY 169) to 0.44 (DOY 201), with an average R^2 value of 0.38 for all the comparisons during the study period.

The slope of the linear regression tends to provide useful information regarding the degree of bias at higher ET and the intercept regarding the magnitude of bias affecting lower ET estimates (Velpuri et al., 2013). Regarding the coefficients of the linear regression between $ET_{RS,MOD16}$ and $ET_{RS,FAO56-PM}$, it can be seen that there is a consistency for the whole study period. In all twelve comparisons the slope of the linear regression is bellow 1 (<1) indicating that MOD16 underestimates higher ET values. The slope coefficient ranges from 0.12 (DOY 209) to 0.94 (DOY 153). Based on the slope coefficient, there are only two DOYs where a linear relationship between the two products is visible, DOY 153 and DOY 161. The rest DOYs have slope coefficients close to 0.5 or lower. Similar with the slope, the intercept of the linear regression is positive in all twelve DOYs. Its values range from 3.26 (DOY 169) to 18.1 (DOY 209) mm/8day.

The RMSE of the 8-day $ET_{RS,MOD16}$ product varied from 3.23 mm/8day (DOY 233) to 9.88 mm/8day (DOY 193), with an average value of 6.58 mm/8day. Lower RMSE values, around 3 mm/8day, were found in the beginning of the growing season (DOY 145) and in the end (DOYs 225 and 233). RMSE was over 6 mm/8day during the rest of the study period.

Looking at the raster maps (Figure 4.11) and the statistical summary of the validation results (Table 4.4), it can be concluded that the $ET_{RS,MOD16}$ product, compared against the $ET_{RS,FAO56-PM}$ product, showed consistently lower ET values during the growing season of 2014, except the 8-day period from 29/7/2014 to 4/8/2014 (DOY 209) where it showed much higher ET. The MBE for all DOYs is -2.93 mm/8day, but if DOY 209 is excluded it reaches the value of -3.81 mm/8day. From the visual interpretation of the raster maps (Figure 4.11) showing the ET difference between the two products ($ET_{RS,FAO56-PM}$-$ET_{RS,MOD16}$), greater differences occur in the period from DOY 153 to DOY 193, where the majority of pixels in the $ET_{RS,MOD16}$ product have lower ET values from 5 to 15 mm/8day. During this period the MBE is are also very high (Table 4.4).

Finally, as mentioned above, the performance of $ET_{RS,MOD16}$ at DOY 209 is erratic resulting in much higher ET values compared to $ET_{RS,FAO56-PM}$. The mean bias error for DOY 209 was 6.75 mm/8day and it resulted in the highest PBIAS among all DOYs, with 52.54% from the observed mean (Table 4.4). The reasons and a possible explanation for this performance are given in the next section, where a point-scale validation of the $ET_{RS,MOD16}$ product is performed.

4.4 Point scale validation

4.4.1 Impact of LAI on MOD16 ET

The $ET_{RS,MOD16}$ and $ET_{RS,FAO56-PM}$ 8-day time series are plotted against the 8-day LAI MOD15A2 time series for the study period (DOY 145-DOY 240) in Figure 4.14. The values obtained from $ET_{RS,MOD16}$ and $ET_{RS,FAO56-PM}$ at each date (DOY) represent the sum of ET corresponding to the next 8-day period, while the LAI values from MOD15A2 at each DOY represent the average of the next 8-day period.

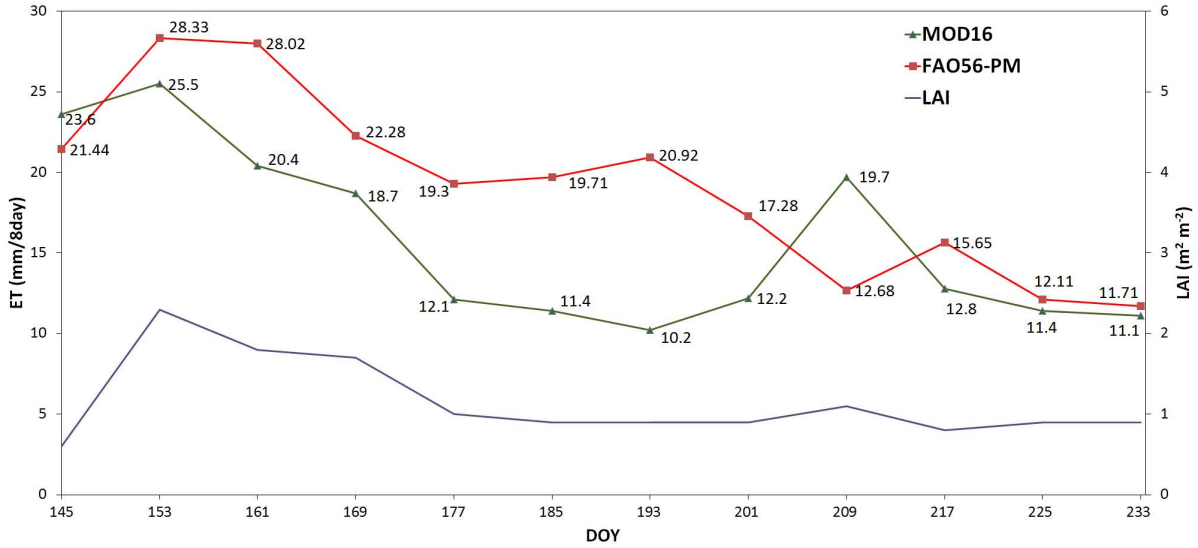

Figure 4.14: 8-day time series of $ET_{RS,MOD16}$ (green line), $ET_{RS,FAO56-PM}$ (red line) and MOD15A2 LAI (purple line) extracted at the pixel of the EC station.

Although the time period is limited and not great fluctuations on the LAI values are expected on a pixel scale, it can be seen in Figure 4.14 that the $ET_{RS,MOD16}$ time series follows the trend of LAI for most of the study period. There is however one 8-day period at 28/07/2014 (DOY 209) which is inconsistent with the LAI. The highest ET from $ET_{RS,MOD16}$ occurs at 02/06/2014 (DOY 153) and the highest LAI is found in the same DOY, with a value slightly over 2 m^2 m^{-2}. The second peak value from $ET_{RS,MOD16}$ is observed at 28/07/2014 (DOY 209), but in this case LAI has a values of approximately 1 m^2 m^{-2}.

The $ET_{RS,FAO56-PM}$ time series has a similar response to LAI as the $ET_{RS,MOD16}$ product. The highest value of ET, 28.33 mm/8day, occurs at 02/06/2014 (DOY 153), as with the MOD16 product. A second peak is observed for the $ET_{RS,FAO56-PM}$ product at 12/07/2014 (DOY 193), with 20.92 mm/8day. At DOY 209 no peak is observed for the $ET_{RS,FAO56-PM}$ product.

4.4.2 Impact of soil water availability on MOD16 ET

Among the most important regulating factors on the rate and amount of soil evaporation is the soil water availability. The available water in the soil can be directly determined by means of rainfall and the soil water content measurements. Thus, to further evaluate the MOD16 algorithm and assess whether it can capture the dynamics of these two parameters in the modelled ET, a comparison against ground-based measurements of rainfall and soil water content was performed.

In Figure 4.15 the time series of $ET_{RS,MOD16}$, 8-day sum of rainfall (mm/8day) and 8-day averaged SWC(%) are plotted. The 8-day $ET_{RS,FAO56-PM}$ time series is also plotted to allow the intercomparison between the two products.

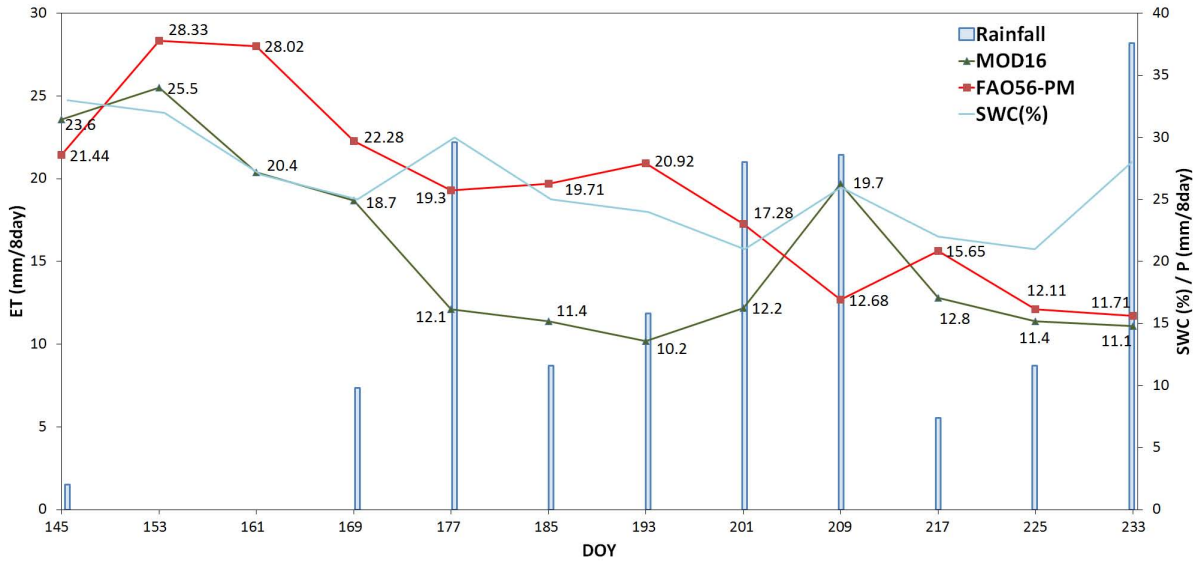

Figure 4.15: 8-day time series of $ET_{RS,MOD16}$ (green line) and $ET_{RS,FAO56-PM}$ (red line) extracted at the pixel of the EC station versus the 8-day sum of rainfall (mm/8day) (blue bars) and the 8-day averaged SWC(%) (light blue line).

Figure 4.15 displays the temporal evolution of $ET_{RS,MOD16}$ and $ET_{RS,FAO56-PM}$ against measured rainfall and soil water content (SWC) at the pixel of the EC station. The increase in soil water content due to rainfall results in higher amount of soil evaporation and thus higher ET rates, but the behaviour of $ET_{RS,MOD16}$ is inconsistent with water availability during the entire study period, except for DOY 209 (28/7/217-4/8/2014). At that 8-day time period the $ET_{RS,MOD16}$ has a peak value of 19.7 mm/8day following the high SWC value of 25%, which was a result of the excess rainfall observed at DOY 209 (approx. 28mm/8day) and DOY 201 (approx. 28mm/8day). The $ET_{RS,FAO56-PM}$ time series is inconsistent with the water availability during the entire study period, since the FAO56-PM method doesn't account for soil evaporation.

To gain a better understanding on how $ET_{RS,MOD16}$ product is capturing the dynamics of water availability and the resulting soil evaporation, it is useful to examine the relative humidity (RH) parameter of the MOD16 algorithm. The soil evaporation component in MOD16 algorithm is based on the relative humidity (RH) of MERRA-GMAO meteorological data and consists of two parts, the evaporation from dry soil surface ($E_{S,dry}$) and the evaporation from wet soil surface ($E_{S,wet}$). The MOD16 algorithm equation for $E_{S,wet}$ (Equation 2.14) suggests that soil evaporation from a saturated surface occurs only when RH>70%. If RH<70%, then no soil evaporation occurs from a wet surface.

Figure 4.16 shows the daily time series of MERRA-GMAO RH (%) as extracted from the pixel of the EC station and measured RH (%).

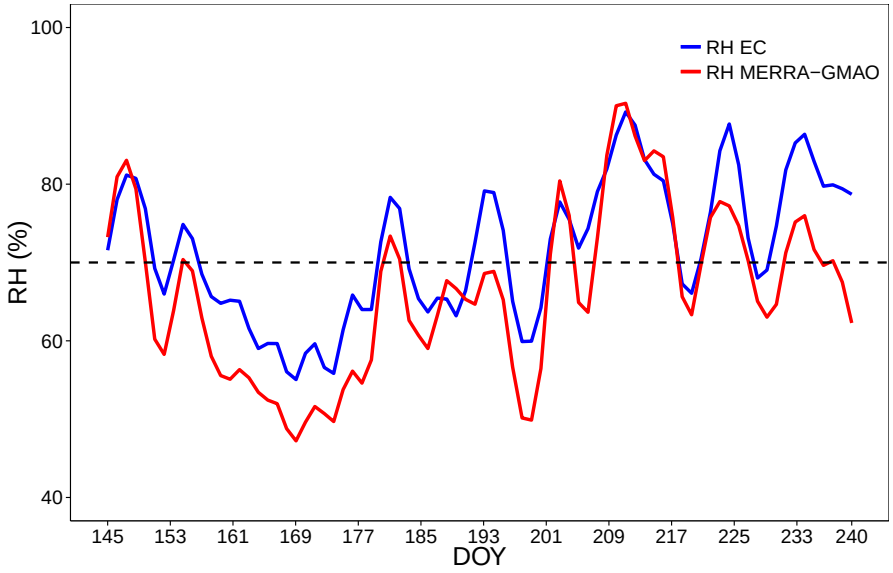

Figure 4.16: Daily time series of MERRA-GMAO RH (%) (red line) and measured RH (%) (blue line). The dashed line indicates 70% of RH.

The time series plot (Figure 4.16) further confirms the good agreement between MERRA-GMAO and measured RH, demonstrated in Section 3.4.4. The average daily RH by MERRA-GMAO exceeded 70% a few times during the study period and in most of these cases it was only for a short time period of 1 to 3 days. The only exception was a 10-day period from DOY 208 to DOY 217 where RH was above 70% for all days, reaching a maximum value of 91% at DOY 211.

The following figure (Figure 4.17) displays the temporal evolution of $ET_{RS,MOD16}$ and $ET_{RS,FAO56-PM}$ against the 8-day average MERRA-GMAO RH(%).

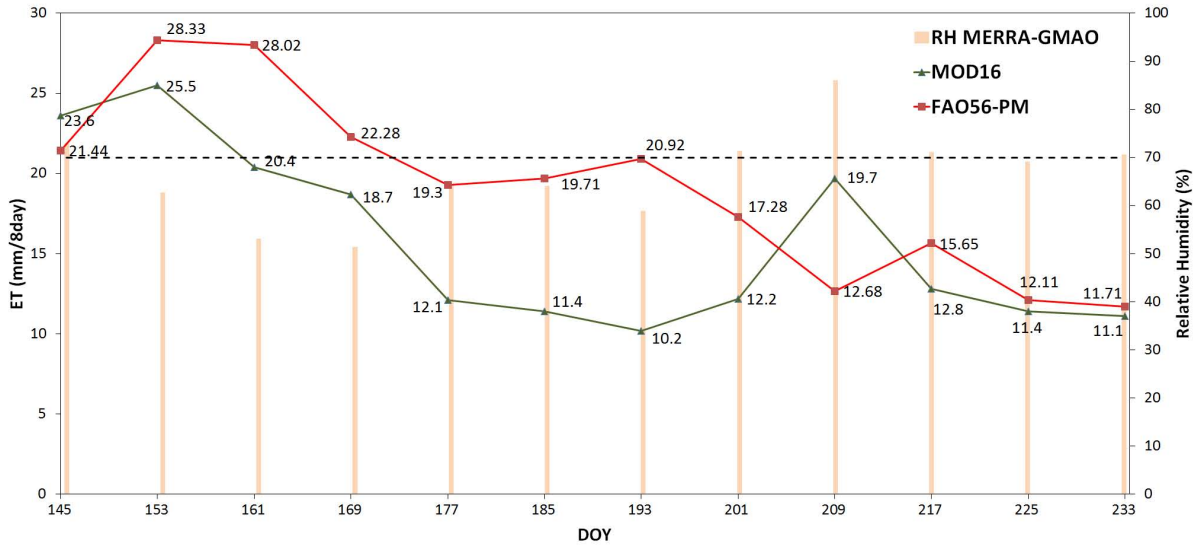

Figure 4.17: 8-day time series of $ET_{RS,MOD16}$ (green line) and $ET_{RS,FAO56-PM}$ (red line) extracted at the pixel of the EC station against the 8-day average MERRA-GMAO RH(%) (light orange bars). The dashed line indicates 70% of RH.

Based on the observation of Figure 4.17 a few high $ET_{RS,MOD16}$ values can be attributed to the MERRA-GMAO RH being over 70%. At DOY 145 (25/5/2014-1/6/2014) $ET_{RS,MOD16}$ had a value of 23.6 mm/8day, the second highest during the study period, while RH had an average value of 73% for the same time period. At DOY 209 (28/7/217-4/8/2014) the peak value of 19.7 mm/8day for $ET_{RS,MOD16}$ can be explained by the fact that RH reached an average 8-day value of 86%, while also staying over 70% for the entire 8-day time period of DOY 209 (Figure 4.16).

The above results show that the MERRA-GMAO relative humidity (RH) parameter used in the MOD16 algorithm for the parametrization of soil moisture proves insufficient. During the period of study only when excess rainfall was observed, from 20/7/204-4/8/2014, the RH could "reproduce" the impact of soil water content on ET.

5 Conclusions

One of the most widely used operational remote sensing ET products is the MODIS Global Terrestrial Evapotranspiration Product (MOD16) providing ET and PET datasets from 2000 until now at 1 km spatial resolution and 8-day or monthly temporal resolution (Yang et al., 2014; Mu et al., 2011). An extended number of validation studies have been published regarding the MOD16 ET product (Mu et al., 2011; Kim et al., 2012; Tang et al., 2015; Ramoelo et al., 2014; Hu et al., 2015; Velpuri et al., 2013), employing a point scale validation approach against eddy covariance (EC) measurements. From these validation studies only few were performed in agricultural areas.

The scope of this thesis was to validate the 8-day MOD16 ET product in an agricultural area, the Marchfeld region in Lower Austria, for most of the growing season of 2014 (May-August). The motivation behind this thesis was to attempt a validation of the MOD16 ET product on a regional scale against validated ET maps with the same spatial and temporal resolution.

The first step of the thesis, and of the validation approach, was to use high-resolution satellite imagery (Landsat-8) and the FAO56-PM "one-step approach", in order to generate hourly ET maps over the Marchfeld region that could be validated against EC measurements of ET. The validation results revealed a high coefficient of determination (R^2) of 0.84 and mean bias error (MBE) of 0.02 mm/hr, proving that the hourly $ET_{RS,FAO56-PM}$ maps could be used as gridded "ground-truth" of ET.

In general, the performance of the FAO56-PM "one-step approach" was satisfactory, reproducing the temporal evolution of ET over most of the study period. It must be notated though that models based on FAO56-PM have a drawback which was evident during this study too. In days with excess rainfall and very high observed ET values, due to soil evaporation, the model couldn't reproduce the dynamics of ET giving low values. These types of models, based on FAO56-PM, should be used only in agricultural areas during the growing season when the crops develop their canopy, covering the entire soil surface, and ET is mainly driven by the transpiration process.

In a second step, the $ET_{RS,FAO56-PM}$ maps were spatially and temporally aggregated in order to match the spatial and temporal resolution of $ET_{RS,MOD16}$. The most important aspect in this procedure was the spatial aggregation of $ET_{RS,FAO56-PM}$ product from the 30 m fine resolution (Landsat) to the 1 km coarse resolution (MODIS). The performance of three spatial aggregation techniques was examined, namely the aggregation with mean value, with median value and the Nearest Neighbour resampling. Based on visual inspection, summary statistics and density plots between the native and aggregated rasters the spatial aggregation with median value performed better, with respect to retaining the statistical characteristics of the native resolution (30 m) ET maps.

Finally, the study compared the 8-day $ET_{RS,MOD16}$ against the validated $ET_{RS,FAO56-PM}$ maps, which were assumed as a type of "ground-truth" data for the entire Marchfeld region. The results would prove the validity of the MOD16 ET product in an agricultural area. The boxplots and the raster maps of the 8-day $ET_{RS,MOD16}$ product showed a low variation of ET values at each DOY, which resulted in a homogeneous pattern of ET across the Marchfeld region at each DOY. The ET values for each DOY ranged not more than 5 mm/8day. The pixel-by-pixel analysis showed a low level of agreement for the entire study period, with average

R^2 of 0.38, and a systematic underestimation of ET by MOD16 in most DOYs of the study period, which ranged from 3.09 mm/8day to 7.78 mm/8day.

The temporal evolution of 8-day $ET_{RS,MOD16}$ was further assessed against input data to the MOD16 algorithm and ground-based ancillary data for the specific location where EC data were available. Specifically, the $ET_{RS,MOD16}$ was compared against the LAI from MOD15A2, the relative humidity (RH) of MERRA-GMAO and ground-based ancillary data, as rainfall and soil water content (SWC). The $ET_{RS,MOD16}$ was consistent with LAI for the entire study period, but did not capture the impact of soil water availability on ET, except for one 8-day period (DOY 209). At that time period the $ET_{RS,MOD16}$ product showed high ET values which were consistent with the daily MERRA-GMAO relative humidity (RH), which is used as a proxy of soil moisture in the MOD16 algorithm.

As part of the validation process followed in this study, the MERRA-GMAO meteorological data used as inputs to the MOD16 algorithm, namely air temperature, relative humidity and net radiation, were compared against ground-based measurements. A high level of agreement based on R^2 and low RMSE values were found for all three variables, indicating that although the MERRA-GMAO datasets have a coarse resolution of $1/2^\circ \times 2/3^\circ$ (approximately 55×75 km) they are not an important source of error in the estimated ET by MOD16 algorithm.

The poor results of the $ET_{RS,MOD16}$ validation indicate that either the $ET_{RS,FAO56-PM}$ product is not as accurate as we expected and cannot be used as gridded "ground-truth" of ET, or that MOD16 ET products have large errors on the estimation of ET in agricultural areas. The results from the point scale validation of the native resolution (30 m) $ET_{RS,FAO56-PM}$ against EC measurements have shown that the $ET_{RS,FAO56-PM}$ maps are in good agreement with observed ET, thus the error introduced from them in the final validation is not significant. The aggregation process followed afterwards could induce significant errors in the final $ET_{RS,FAO56-PM}$ (1 km) used for the validation of $ET_{RS,MOD16}$.
Concerning the MOD16 ET product, some studies (Di et al., 2015; Yang et al., 2015) have suggested that the current parametrization of the MOD16 algorithm is not "suitable" for the estimation of ET across all types of climate and land cover. Specifically, Tang et al. (2015) noted that there are limitations on using ET from MOD16 in irrigated agricultural areas, like the Marchfeld region. In a direction to improve the MOD16 algorithm, recommendations are made concerning the integration of a soil moisture parameter with the consideration of rainfall. Furthermore, an important source of uncertainty is the issue of scale on ET estimation with coarse resolution products, as the MOD16. All the global available RS-based ET datasets have a spatial resolution of 1 km or coarser, which is significantly larger than the agricultural fields. As a result these ET products fail to assess crop-specific ET (Biggs et al., 2015). Finally, the pixel-by-pixel comparison between Landsat-based and MODIS-based ET products leads to significant discrepancies due to georeferencing disagreement and different point-spread functions (PSF) between imagery from the two different sensors.

Regional and global estimates of evapotranspiration are important for understanding water and energy balances. In the latest years, automated methods have been developed that use routinely available remotely sensed data to provide continuous time series of ET over large areas, which are useful for water resources management, irrigation advisory services and drought impact assessment. These operational remote sensing methods and products estimate ET at moderate spatial resolution on regional and global coverage and therefore could prove valuable in the future.

The biggest issue regarding these methods and products is their accuracy on estimating ET. More evaluation studies should be performed across multiple temporal and spatial scales and in a variety of ecosystems globally. The results of these evaluations and the intercomparison of products will further improve ET estimations on regional and global scales, will determine which remotely sensed method/product should be used over a given area providing better estimates and will finally allow the use of remotely sensed ET products with confidence.

Bibliography

Allen, R. G. (2000). Using the FAO-56 dual crop coefficient method over an irrigated region as part of an evapotranspiration intercomparison study. *Journal of Hydrology*, 229:27–41.

Allen, R. G., Pereira, L., Raes, D., and Smith, M. (1998). Crop evapotranspiration: Guidelines for computing crop requirements. *Irrigation and Drainage Paper No. 56, FAO*, (56):300.

Bian, L. and Butler, R. (1999). Comparing effects of aggregation methods on statistical and spatial properties of simulated spatial data. *Photogrammetric Engineering and Remote Sensing*, 65(1):73–84.

Biggs, T., Petropoulos, G., Velpuri, N., Marshall, M., Glenn, E., Nagler, P., and Messina, A. (2015). Remote Sensing of Actual Evapotranspiration from Croplands. In *Remote Sensing of Water Resources, Disasters, and Urban Studies*, Remote Sensing Handbook, pages 59–99. CRC Press.

Brutsaert, W. (1982). *Evaporation into the Atmosphere: Theory, History and Applications*. Environmental Fluid Mechanics. Springer Netherlands.

Cleugh, H., Leuning, R., Mu, Q., and Running, S. W. (2007). Regional evaporation estimates from flux tower and MODIS satellite data. *Remote Sensing of Environment*, 106(3):285–304.

Clevers, J. (1989). Application of a weighted infrared-red vegetation index for estimating leaf Area Index by Correcting for Soil Moisture. *Remote Sensing of Environment*, 29(1):25–37.

Di, S.-C., Li, Z.-L., Tang, R., Wu, H., Tang, B.-H., and Lu, J. (2015). Integrating two layers of soil moisture parameters into the MOD16 algorithm to improve evapotranspiration estimations. *International Journal of Remote Sensing*, 36(19-20):4953–4971.

Dingman, S. L. (2001). Evapotranspiration. In *Physical Hydrology*, chapter 7, pages 272–324. Prentice Hall.

D'Urso, G. (2001). *Simulation and Management of on-demand irrigation systems : A combined agrohydrological and remote sensing approach*. PhD thesis, Wageningen Agricultural University.

D'Urso, G., Richter, K., Calera, A., Osann, M. A., Escadafal, R., Garatuza-Pajan, J., Hanich, L., Perdigão, A., Tapia, J. B., and Vuolo, F. (2010). Earth Observation products for operational irrigation management in the context of the PLEIADeS project. *Agricultural Water Management*, 98(2):271–282.

Ershadi, A., McCabe, M., Evans, J., and Walker, J. (2013). Effects of spatial aggregation on the multi-scale estimation of evapotranspiration. *Remote Sensing of Environment*, 131:51–62.

Fisher, J. B., Tu, K. P., and Baldocchi, D. D. (2008). Global estimates of the land-atmosphere water flux based on monthly AVHRR and ISLSCP-II data, validated at 16 FLUXNET sites. *Remote Sensing of Environment*, 112(3):901–919.

Freyer, B., Friedel, J., Surböck, A., Heinzinger, M., and Schauppenlehner, T. (2010). ÖPUL-Evaluierung LE07-13: Bewertung des viehlosen biologischen Ackerbaus und seiner agrarökologischen Leistungen im österreichischen Trockengebiet (Zwischenbericht). Technical report, Bundesministerium für Land- und Forstwirtschaft, Umwelt- und Wasserwirtschaft.

Geosystem Gmbh (2014). ATCOR for Imagine 2014, User Manual.

Glenn, E. P., Huete, A. R., Nagler, P. L., Hirschboeck, K. K., and Brown, P. (2007). Integrating Remote Sensing and Ground Methods to Estimate Evapotranspiration. *Critical Reviews in Plant Sciences*, 26:139–168.

Glenn, E. P., Nagler, P. L., and Huete, A. R. (2010). Vegetation Index Methods for Estimating Evapotranspiration by Remote Sensing. *Surveys in Geophysics*, 31:531–555.

Glenn, E. P., Neale, C. M. U., Hunsaker, D. J., and Nagler, P. L. (2011). Vegetation index-based crop coefficients to estimate evapotranspiration by remote sensing in agricultural and natural ecosystems. *Hydrological Processes*, 25(26):4050–4062.

Gowda, P. H., Chavez, J. L., Colaizzi, P. D., Evett, S. R., Howell, T. A., and Tolk, J. A. (2008). ET mapping for agricultural water management: Present status and challenges. *Irrigation Science*, 26:223–237.

Hong, S.-h., Hendrickx, J. M. H., and Borchers, B. (2009). Up-scaling of SEBAL derived evapotranspiration maps from Landsat (30 m) to MODIS (250 m) scale. *Journal of Hydrology*, 370(1-4):122–138.

Hu, G., Jia, L., and Menenti, M. (2015). Comparison of MOD16 and LSA-SAF MSG evapotranspiration products over Europe for 2011. *Remote Sensing of Environment*, 156:510–526.

Irmak, A., Allen, R. G., Kjaersgaard, J., Huntington, J., Kamble, B., Trezza, R., and Ratcliffe, I. (2012). Operational Remote Sensing of ET and Challenges. *Evapotranspiration - Remote Sensing and Modeling*.

Kalma, J. D., McVicar, T. R., and McCabe, M. F. (2008). Estimating land surface evaporation: A review of methods using remotely sensed surface temperature data. *Surveys in Geophysics*, 29:421–469.

Kim, H. W., Hwang, K., Mu, Q., Lee, S. O., and Choi, M. (2012). Validation of MODIS 16 global terrestrial evapotranspiration products in various climates and land cover types in Asia. *KSCE Journal of Civil Engineering*, 16(2):229–238.

Kirchner, M. and Schmid, E. (2013). Trade policy and climate change impacts on regional land use and environment. *Jahrbuch der ÖGA (Österreichische Gesellschaft für Agrarökonomie)*, 22(2):23–32.

Li, Z. L., Tang, R., Wan, Z., Bi, Y., Zhou, C., Tang, B., Yan, G., and Zhang, X. (2009). A review of current methodologies for regional Evapotranspiration estimation from remotely sensed data. *Sensors*, 9:3801–3853.

Liang, S., Fang, H., and Chen, M. (2001). Atmospheric correction of Landsat ETM+ land surface imagery. I.\nMethods. *IEEE Transactions on Geoscience and Remote Sensing*, 39(11):2490–2498.

Liang, S. L., Fang, H. L., Chen, M. Z., Shuey, C. J., Walthall, C., Daughtry, C. S. T., Morisette, J. T., Schaaf, C., and Strahler, A. H. (2002). Validating MODIS land surface reflectance and albedo products: methods and preliminary results. *Remote Sensing Of Environment*, 83:149–162.

Los, S. O., Pollack, N. H., Parris, M. T., Collatz, G. J., Tucker, C. J., Sellers, P. J., Malmström, C. M., DeFries, R. S., Bounoua, L., and Dazlich, D. a. (2000). A Global 9-yr Biophysical Land Surface Dataset from NOAA AVHRR Data. *Journal of Hydrometeorology*, 1(2):183–199.

Lucchesi, R. (2012). File Specification for MERRA Products. GMAO Office Note No. 1 (Version 2.3). 1(1).

McCabe, M. F. and Wood, E. F. (2006). Scale influences on the remote estimation of evapotranspiration using multiple satellite sensors. *Remote Sensing of Environment*, 105(4):271–285.

Moene, A. F. and van Dam, J. C. (2014). *Transport in the atmosphere-vegetation-soil continuum*. Cambridge University Press.

Monteith, J. L. (1965). Evaporation and environment. *Symposia of the Society for Experimental Biology*, 19:205–234.

Mu, Q., Jones, L. a., Kimball, J. S., McDonald, K. C., and Running, S. W. (2009). Satellite assessment of land surface evapotranspiration for the pan-Arctic domain. *Water Resources Research*, 45(9):1–20.

Mu, Q., Zhao, M., Heinsch, F. A., Liu, M., Tian, H., and Running, S. W. (2007). Evaluating water stress controls on primary production in biogeochemical and remote sensing based models. *Journal of Geophysical Research: Biogeosciences*, 112(1):1–13.

Mu, Q., Zhao, M., and Running, S. W. (2011). Improvements to a MODIS global terrestrial evapotranspiration algorithm. *Remote Sensing of Environment*, 115(8):1781–1800.

Nagler, P. L., Glenn, E. P., Lewis Thompson, T., and Huete, A. (2004). Leaf area index and normalized difference vegetation index as predictors of canopy characteristics and light interception by riparian species on the Lower Colorado River. *Agricultural and Forest Meteorology*, 125(1-2):1–17.

Neale, C. M. U., Bausch, W. C., and Heermann, D. F. (1989). Development of reflectance-based crop coefficients for corn. *Transactions of the American Society of Agricultural Engineers*, 32(6):1891–1899.

Neugebauer, N. (2013). *Estimation of crop water requirements based on remote sensing data: A case study of the Marchfeld region in 2010*. Msc thesis, University of Natural Resources and Life Sciences, Vienna.

Overgaard, J., Rosbjerg, D., and Butts, M. B. (2005). Land-surface modelling in hydrological perspective. *Biogeosciences Discussions*, 2:1815–1848.

Penman, H. L. (1948). Natural Evaporation from Open Water, Bare Soil and Grass. *Proceedings of the Royal Society of London. Series A, Mathematical and Physical Sciences*, 193(1032):120–145.

Pereira, L. S., Allen, R. G., Smith, M., and Raes, D. (2014). Crop evapotranspiration estimation with FAO56: Past and future. *Agricultural Water Management*, pages 1–16.

Petropoulos, G., Carlson, T., Wooster, M., and Islam, S. (2009). A review of Ts/VI remote sensing based methods for the retrieval of land surface energy fluxes and soil surface moisture. *Progress in Physical Geography*, 33(2):224–250.

Petropoulos, G. P. (2013). *Remote Sensing of Energy Fluxes and Soil Moisture Content*. CRC Press.

Ramoelo, A., Majozi, N., Mathieu, R., Jovanovic, N., Nickless, A., and Dzikiti, S. (2014). Validation of Global Evapotranspiration Product (MOD16) using Flux Tower Data in the African Savanna, South Africa. *Remote Sensing*, 6(8):7406–7423.

Richter, K., Rischbeck, P., Eitzinger, J., Schneider, W., Suppan, F., and Weihs, P. (2008). Plant growth monitoring and potential drought risk assessment by means of Earth observation data. *International Journal of Remote Sensing*, 29(17-18):4943–4960.

Richter, R. (1996). A spatially adaptive fast atmospheric correction algorithm. *International Journal of Remote Sensing*, 17(6):1201–1214.

Richter, R. (1998). Correction of Satellite Imagery Over Mountainous Terrain. *Applied Optics*, 37(18):4004.

Richter, R. (2001). Atmospheric Correction Methodology for Imaging Spectrometer Data. In Wooding, M. and Harris, R., editors, *The Digital Airborne Spectrometer Experiment (DAISEX)*, volume 499 of *ESA Special Publication*, page 97.

Rienecker, M. M., Suarez, M. J., Gelaro, R., Todling, R., Bacmeister, J., Liu, E., Bosilovich, M. G., Schubert, S. D., Takacs, L., Kim, G. K., Bloom, S., Chen, J., Collins, D., Conaty, A., Da Silva, A., Gu, W., Joiner, J., Koster, R. D., Lucchesi, R., Molod, A., Owens, T., Pawson, S., Pegion, P., Redder, C. R., Reichle, R., Robertson, F. R., Ruddick, A. G., Sienkiewicz, M., and Woollen, J. (2011). MERRA: NASA's modern-era retrospective analysis for research and applications. *Journal of Climate*, 24(14):3624–3648.

Senay, G. B., Leake, S., Nagler, P. L., Artan, G., Dickinson, J., Cordova, J. T., and Glenn, E. P. (2011). Estimating basin scale evapotranspiration (ET) by water balance and remote sensing methods. *Hydrological Processes*, 25(26):4037–4049.

Su, H., McCabe, M. F., Wood, E. F., Su, Z., and Prueger, J. H. (2005). Modeling Evapotranspiration during SMACEX: Comparing Two Approaches for Local- and Regional-Scale Prediction. *Journal of Hydrometeorology*, 6(6):910–922.

Su, Z., Pelgrum, H., and Menenti, M. (1999). Aggregation effects of surface heterogeneity in land surface processes. *Hydrology and Earth System Sciences*, 3(4):549–563.

Tang, R., Shao, K., Li, Z.-l., Wu, H., Tang, B.-h., Zhou, G., and Zhang, L. (2015). Multiscale Validation of the 8-day MOD16 Evapotranspiration Product Using Flux Data Collected in China. *IEEE Journal of Selected Topics in Applied Earth Observations and Remote Sensing*, pages 1–9.

Vanino, S., Pulighe, G., Nino, P., De Michele, C., Bolognesi, S., and DUrso, G. (2015). Estimation of Evapotranspiration and Crop Coefficients of Tendone Vineyards Using Multi-Sensor Remote Sensing Data in a Mediterranean Environment. *Remote Sensing*, 7(11):14708–14730.

Velpuri, N. M., Senay, G. B., Singh, R. K., Bohms, S., and Verdin, J. P. (2013). A comprehensive evaluation of two MODIS evapotranspiration products over the conterminous United States: Using point and gridded FLUXNET and water balance ET. *Remote Sensing of Environment*, 139:35–49.

Verstraeten, W. W., Veroustraete, F., and Feyen, J. (2008). Assessment of Evapotranspiration and Soil Moisture Content Across Different Scales of Observation. *Sensors*, 8(ii):70–117.

Vuolo, F., DUrso, G., De Michele, C., Bianchi, B., and Cutting, M. (2015). Satellite-based irrigation advisory services: A common tool for different experiences from Europe to Australia. *Agricultural Water Management*, 147:82–95.

Wang, K. and Dickinson, R. E. (2012). A review of global terrestrial evapotranspiration: observation, modelling, climatology, and climatic variability. *Review of Geophysics*, 50(2):1–54.

Yang, Y., Guan, H., Shang, S., Long, D., and Simmons, C. T. (2014). Toward the use of the MODIS et product to estimate terrestrial GPP for nonforest ecosystems. *IEEE Geoscience and Remote Sensing Letters*, 11(9):1624–1628.

Yang, Y., Long, D., Guan, H., Liang, W., Simmons, C., and Batelaan, O. (2015). Comparison of three dual-source remote sensing evapotranspiration models during the MUSOEXE-12 campaign: Revisit of model physics. *Water Resources Research*, 51(5):3145–3165.

Zhao, M., Heinsch, F. A., Nemani, R. R., and Running, S. W. (2005). Improvements of the MODIS terrestrial gross and net primary production global data set. *Remote Sensing of Environment*, 95(2):164–176.